AIAA AVIATION Forum
12-16 June 2023, San Diego, CA and Online
AIAA AVIATION 2023 Forum
10.2514/6.2023-3337

Pressure Gradient Effects on Boundary Layer Superstructures

Humza Butt*, Shishir Damani†, Shreyas Chaware‡ Máté Szőke§, Surabhi Srivastava ¶, Todd K. Lowe‖, and William Devenport**
Virginia Polytechnic Institute and State University, Blacksburg, Virginia, 24060

Alistair Hales ††, Matthew Colbrook ‡‡, Lorna J. Ayton §§
University of Cambridge, Cambridge, UK CB3 0WA

Spanwise homogeneous turbulent boundary layers convect groups of flow structures that move with similar momentum, often called coherent structures. These coherent structures remain statistically similar as they get convected downstream. The length scales of such coherent structures vary with the wall-normal distance of the boundary layer. Large-scale motions on the order of 20δ, often termed superstructures, are conjectured to be present in the outer layer. However, Particle Image Velocimetry (PIV) data acquired at the bottom of the logarithmic layer of the boundary layer provides evidence of the existence of superstructures in the overlap region. Their presence in the close vicinity of the wall makes them a strong candidate to be the prime contributors to the low-wavenumber pressure fluctuations in a smooth wall. A discussion on the fundamental nature of these superstructures in the smooth-wall turbulent boundary layer is presented, followed by the flow field's decomposition into its streamwise wavenumber and frequency components. The experimental data is also analyzed using a novel dynamic mode decomposition technique, ResDMD. This decomposition approach differs from other known techniques due to error control, verification (e.g., of dictionaries) and convergence theorems. This technique was used to uncover the transient behavior within the system and identify turbulence events based on their length scales and convection velocities. The extent of the streamwise flow homogeneity is also discussed. Evidence of high spectral levels at low-wavenumbers confirms the role of superstructures in containing a significant fraction of the turbulence energy. The streamwise wavenumber-frequency spectra of the pressure fluctuations at sub-convective wavenumbers support this.

I. Nomenclature

u_i	=	fluctuating velocity component
U_i	=	mean velocity component
C_p	=	pressure coefficient
x, x_1	=	streamwise direction
y, x_2	=	wall-normal direction
z, x_3	=	spanwise direction
f_s	=	sampling frequency
c	=	airfoil chord
ϕ_{uu}	=	spectrum of the streamwise velocity fluctuations
ϕ_{pp}	=	spectrum of the pressure fluctuations

*PhD Candidate, Aerospace and Ocean Engineering, Blacksburg, VA, USA, AIAA Student Member
†PhD Candidate, Aerospace and Ocean Engineering, Blacksburg, VA, USA, AIAA Student Member
‡Masters Student, Aerospace and Ocean Engineering, Blacksburg, VA, USA,
§Senior Research Associate, Aerospace and Ocean Engineering, Blacksburg, VA, USA, AIAA Member
¶Masters Student, Aerospace and Ocean Engineering, Blacksburg, VA, USA, AIAA Student Member
‖Professor, Aerospace and Ocean Engineering, Blacksburg, VA, USA, AIAA Associate Fellow
**Crofton Professor in Engineering, Aerospace and Ocean Engineering, Blacksburg, VA, USA, AIAA Fellow
††PhD Student, Department of Applied Mathematics and Theoretical Physics, Cambridge, UK
‡‡Assistant Professor, Department of Applied Mathematics and Theoretical Physics, Cambridge, UK
§§EPSRC Early Career Fellow, Department of Applied Mathematics and Theoretical Physics, Cambridge, UK

h = height of laser sheet
k = angular wavenumber
ω = angular frequency
α = angle of attack
ν = kinematic viscosity of air
u_τ = friction velocity
L_{ij} = integral length-scale of velocity u_i in the x_j direction

II. Introduction

Turbulence is one of the most frequently encountered and widely studied flow phenomena in aerospace and ocean engineering. Any device or vehicle in motion will most likely interact with turbulent flow during its mission. The interaction of an aerodynamic surface with an oncoming turbulent flow gives rise to pressure fluctuations on that surface. This is detected as near and far-field sound, and it can prove detrimental for vehicles dedicated to defense-related missions. These pressure fluctuations also give rise to structural vibrations and can result in a structural failure of a specific component or surface of the vehicle. It is, therefore, essential to understand the quantitative behavior of these surface pressure fluctuations and identify the flow sources that give rise to these phenomena.

The wavenumber-frequency spectrum of the pressure fluctuations ϕ_{pp} provide an excellent statistical tool to allow the spatio-temporal decomposition of the energy contained in these pressure fluctuations under the influence of turbulent flows. The direct relation of these spectra to the two-point space-time correlation of the pressure fluctuations makes it a favorable tool for such an investigation. Equation 1 provides the mathematical definition of these spectra for a two-dimensional homogeneous turbulent boundary layer.

$$\phi_{pp}(\mathbf{k}, \omega) = \frac{1}{(2\pi)^3} \int_{-R_\infty}^{+R_\infty} \int_{-R_\infty}^{+R_\infty} \int_{-T_\infty}^{+T_\infty} R_{pp}(\Delta\mathbf{x}, \tau) e^{-i(\mathbf{k}.\Delta\mathbf{x} - \omega t)}\, d\tau dx dz \tag{1}$$

Here, **k** represents the wavenumber vector, ω represents the frequency, Δx shows the spatial separation, τ represents the time delay, and R_{pp} represents the correlation of the pressure fluctuations also defined in Equation 2.

$$R_{pp}(\Delta\mathbf{x}, \tau) = E[p(x, z, t)\ p(x', z', t + \tau)] \tag{2}$$

A schematic of this wavenumber-frequency spectra is also shown in Figure 1.

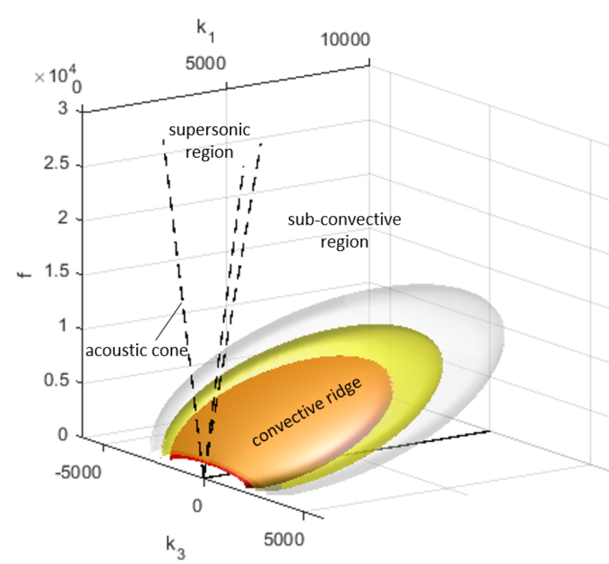

Fig. 1 Schematic of the streamwise-spanwise wavenumber-frequency spectra of the smooth wall-pressure fluctuations [1]

In Figure 1, the horizontal axes represent the streamwise and spanwise wavenumbers, while the vertical axis represents frequency. Three distinct features of the spectrum space are also labeled in the figure. The acoustic cone represents the energy traveling at the sound speed. Anything that has an apparent faster speed is encapsulated by the acoustic cone and is termed the 'supersonic region.' The sources of the pressure fluctuations being convected downstream at the convection velocity leave their footprints on the convective ridge. Three distinct contour levels of the convective sources are presented. Their slope in the streamwise (k_1) direction represents the convection velocity in meters per second. A peculiar region of interest is the sub-convective region, enclosed between the convective ridge and the acoustic cone. The sources that give rise to elevated spectral levels in this region have been a source of debate among the investigators of this problem and have been a subject of research for past many decades. Experimental campaigns started in the mid-twentieth century with a series of tests conducted by Willmarth, who used pressure sensing films in a flat plate to correlate the pressure fluctuations experienced on different parts of the plate [2]. Kraichnan proposed an analytical scheme to qualitatively describe the role of wall-bounded turbulent flow to the induced pressure fluctuations but highlighted a dearth of experimental data and a limited range of experimentally tested wavenumbers [3]. Corcos proposed semi-empirical models of the pressure fluctuations [4] and Chase [5, 6], which used boundary layer parameters to collapse the wavenumber-frequency spectra of the pressure fluctuations. A number of these models were compared by Graham [7] and Blake [8].

Inspired by a recent study on acoustic metamaterials, a novel non-intrusive scheme has been devised to tackle the spatial aliasing problem in the measurements of surface pressure fluctuations. This involves an array of cavity-based sensors, covered with Kevlar, used as pressure sensors specifically designed to target low-wavenumber fluctuations. The details of the cavity-based sensors, the design, and the calibration of the pressure-sensing array have been discussed by Damani et. al. [9]. The experimental results at varying Reynolds numbers and mean-pressure gradients have also been documented by Butt et. al. [10]. The pressure-sensing array presented in these two studies resolves the convective ridge and successfully captures the supersonic elements of the pressure field within the acoustic cone. Spectral levels associated with low-wavenumbers were identified to be about 30 dB below the convective pressure fluctuations. These results show promising advancements toward measuring wall-pressure fluctuations with reduced aliasing, though they are not yet perfected. Moreover, there needs to be more discussion on the flow sources that give rise to these pressure fluctuations.

The sources of wall-pressure fluctuations within a turbulent boundary layer have been under debate by conflicting theories. Several attempts to visualize the flow near smooth (and sometimes rough) walls were made to identify the nature of the flow in such regime Grant [11] Blake [12]. Kovasznay [13] reviewed the earlier understanding of the turbulent boundary layer and discussed the presence of near-wall vortical motions, which may have larger streamwise length scales as predicted by previous studies. These were popularized by Townsend [14] as large eddies. Up until the end of the twentieth century, Large-Scale Motions (LSMs) were explored using hot-wire probes and Direct Numerical Simulations (DNS), with explanations emerging from theoretical modeling studies as the one explained by Zhou et. al. [15].

The presence of organized motions in turbulent pipe flows, distinctively larger than the previously discussed LSMs, (i.e., on the order of 12-14 pipe radii), were observed using hot-wire probes by Kim and Adrian [16]. Similar observations were made by del Alamo et. al. [17], who used numerical simulations in a turbulent channel flow to show the presence of two distinct eddy families (coherent structures distinct from one another based on their length scales). The advent of more sophisticated flow visualization techniques, like Laser Doppler Velocimetry (LDV) and Particle Image Velocimetry (PIV) revolutionized the research methods among the fluid dynamics community. In an attempt to visualize the vortex packets (as the one explained in [15]), wall-parallel stereoscopic PIV was conducted in the logarithmic layer of the turbulent boundary layer by Ganapathisubramani [18, 19]. Packets of streamwise oriented vortices larger than the boundary layer thickness were discovered. Showing their dominant contribution to the overall Reynolds shear stress of the flow (more than 25%), they were considered vital for the turbulence transport mechanism. This inspired further studies to investigate the existence and nature of large-scale coherent motions in turbulent boundary layers. However, until this time, these large structures were considered grouped packets of ordered hairpin vortices. The scaling of the measure statistics, such as streamwise velocity spectra or correlation functions, on the inner-wall units (u_τ, ν, etc.) suggested a passive role of these large-scale structures on all Reynolds numbers.

Detailed boundary layer measurements at various wall-normal heights using hot-wire arrays at relatively high Reynolds numbers ($Re_\tau = 1000, 7300$) allowed the scaling of the premultiplied velocity spectra ($\phi_{u_1 u_1}$) at both inner and outer scales [20, 21]. Distinct peaks in the streamwise velocity spectra were observed in the viscous sublayer and the boundary layer's logarithmic layer. The bimodal nature of the spectra occurring at two different length scales confirmed the large-scale organized motions in smooth wall turbulent boundary layers. These organized families were termed' superstructures' to separate these large-scale coherent motions in boundary layer flows from the wall-bounded channel or pipe flows.

This study aims to identify the large-scale coherent structures near a smooth wall that can be attributed to the induced low wavenumber wall-pressure fluctuations. Time-Resolved Particle Image Velocimetry (TR-PIV) allows the visualization of a turbulent boundary layer and its associated flow characteristics. As suggested by the plethora of literature cited earlier, these structures can be as large as multiple boundary layer thicknesses in the streamwise direction, and they can have a spanwise-meandering nature [20–22]. Therefore, a wall-parallel flow-aligned PIV plane in the lower end of the boundary layer's logarithmic region ($y^+ \approx 110 - 157$) has been selected for the analysis. The physical limitation intrinsic to the experimental setup makes it difficult for the laser sheet to align any closer to the wall, making the inner part of the boundary layer inaccessible. Nevertheless, such a measurement can allow the quantification of streamwise length scales of turbulent flow and a deeper understanding of the meandering nature caused by the differences in mean-pressure gradients. Moreover, streamwise wavenumber-frequency spectra can also allow a direct comparison between the velocity and pressure measurements made by the array used in [9] and [10].

An additional analysis on the flow visualization data is performed with dynamic mode decomposition to gain more insight into the underlying behaviors of these superstructures. This technique takes nonlinear discretized dynamical systems and linearizes them by looking at the Koopman operator for the system and its associated eigenfunctions and eigenvalues. As explained in [23, 24], many variants of Koopman algorithms exist. The Residual Dynamic Mode Decomposition (ResDMD) method is chosen for this purpose, which has already been used to analyze turbulence within a wall-jet boundary layer flow [25]. With the introduction of convergence theorems, this algorithm differs from other popular DMD algorithms thanks to error control of modes via assigning a residual. In [25], nonlinear features of the flow were captured thanks to the choice of basis functions within the algorithm, while important transient behaviors of the flow are seen within the modes with low residuals. An initial investigation demonstrates how ResDMD can reliably pick out coherent structures and also reproduce turbulence statistics from the experimental data obtained in a wind tunnel.

III. Experimental Setup

A. Stability Wind Tunnel

The experiments are conducted in the Virginia Tech Stability Wind Tunnel (VT SWT), a closed-circuit suction type, single return, subsonic wind tunnel. The wind tunnel provides flow speeds up to 80 m/s (5 million Reynolds number per meter), and a clean flow with turbulence levels of 0.01% at 20 m/s and 0.023% at 70 m/s. Figure 2 shows a schematic of the wind tunnel.

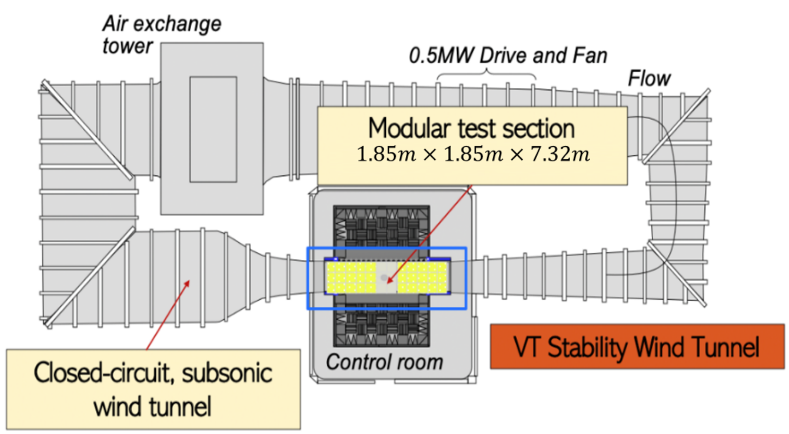

Fig. 2 Schematic of the Virginia Tech Stability Wind Tunnel

The wind tunnel provides a large test section with a cross-sectional area of 1.85 m × 1.85 m and a streamwise length of 7.32 m. All four test section walls are made of 0.61 m × 0.61 m aluminum panels, which can be removed easily. This modular nature of the test section allows easy installation of various models and instrumentation along the wall, floor, and ceiling. Figure 3 shows a schematic of the SWT test section. Here, the flow enters the test section from the left and leaves to the right. The two horizontal lines show the starboard, the port side of the test section, and the general coordinate system. All four walls of the test section consist of three rows of aluminum panels containing 10 panels in each row (30 panels on each wall). The global origin is selected to be the mid-span point of the upstream edge of the first panel in the middle row of the port wall, with the positive x direction pointing downstream and positive y pointing normal and away from the wall. Flow is tripped near the end of the contraction chamber using a zig-zagged strip that is 3.18 mm tall (normal to the wall) and 20.39 mm wide (streamwise direction). The sharp zig-zag pattern has an internal angle of 27.6° and is located at a distance of 3.58 m upstream of the global origin.

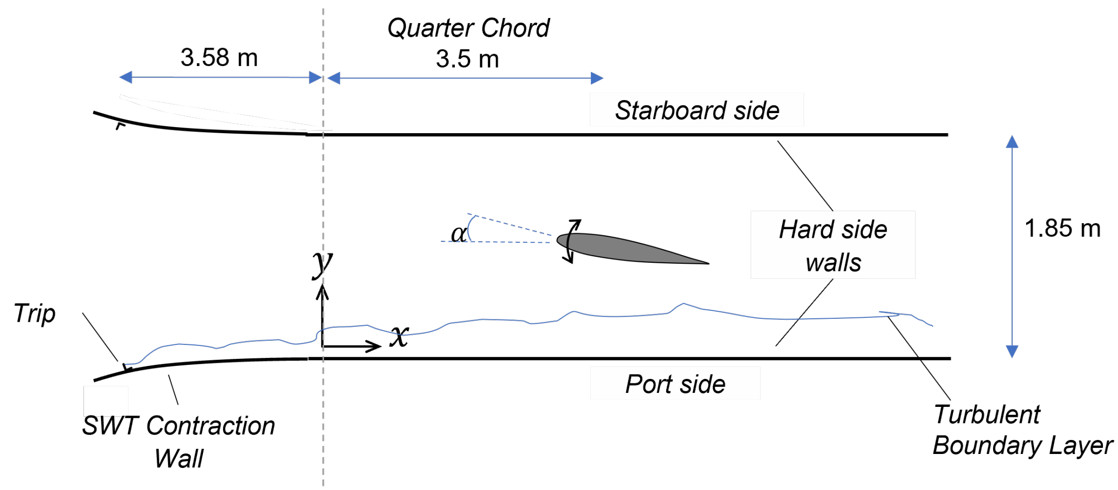

Fig. 3 Schematic of the VT SWT Test-Section.

A 0.914 m chord NACA 0012 airfoil that spans from the floor to the ceiling is mounted such that the leading edge is 3.22 m away from the origin. The change in the angle of attack of this airfoil creates mean pressure gradients on the side walls. A distribution of the pressure coefficient on the port-side wall with the change in airfoil angle of attack is presented in Figure 4. For this figure, the airfoil was made to change its angle of attack from -10° to +12° in increments of 2° as shown by the key. The details of the test section, airfoil, mean pressure profiles, and the tripping mechanism have also been extensively covered in [10].

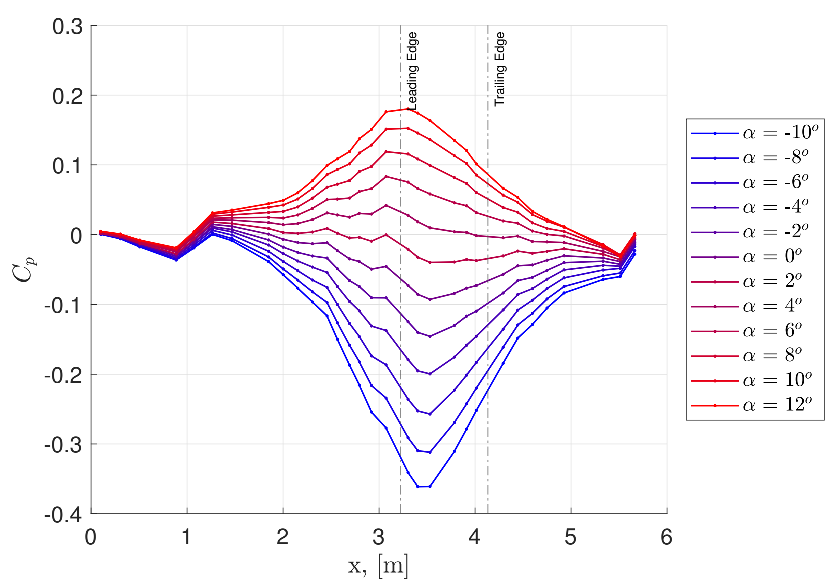

Fig. 4 Pressure coefficient distribution along the mid-span of the port side wall of the Stability Wind Tunnel

In Figure 4, the horizontal axis depicts the streamwise distance on the port wall of the test section, while the vertical axis shows the mean-pressure coefficient. The projection of the leading and trailing edges of the NACA 0012 airfoil on the port wall, in its zero-degree angle of attack configuration, is shown with black dotted-dashed lines. For convention, the airfoil is considered to be pitching down (negative angle of attack) when the leading edge is facing the port wall.

B. Flow Conditions

Flow conditions provided by the wind tunnel were measured using static pressure taps mounted flushed with the inner linings of the walls. Data acquisition schemes and specifications of the instrumentation used in the experiment have previously been discussed in great detail by Butt et. al. [10]. For the results presented in this paper, all the flow measurements were acquired between $x = 2.69$ m and $x = 3.29$ m at the port wall of the test section. Referring to Figure 4, this region is upstream of the airfoil's leading edge, and hence the mean-pressure gradient remains consistently linked with the airfoil's angle of attack. In other words, at this location upstream of the airfoil, the negative values of α always correspond to a favorable pressure gradient and vice versa. While the general effect of the pressure gradients, represented by the sign of the Clauser boundary layer parameter (β), remains consistent for the measurement locations, their specific values vary.

The analyses shown in this paper will correspond to only three out of the 12 cases shown in Figure 4: -10°, 0°, and +12°. For all figures presented in this paper, the adverse pressure gradient cases (+12°, APG) will be presented in red, the small (near-zero) pressure gradient cases (0°, SPG) will be presented in black, and the favorable pressure gradient cases (-10°, FPG) will be shown in blue. Moreover, the location of the upstream edge of the FOV (i.e., $x = 2.69$ m) will be referred to as a reference location x_0. Figure 5 shows the boundary layer profile for the three pressure gradient cases under consideration.

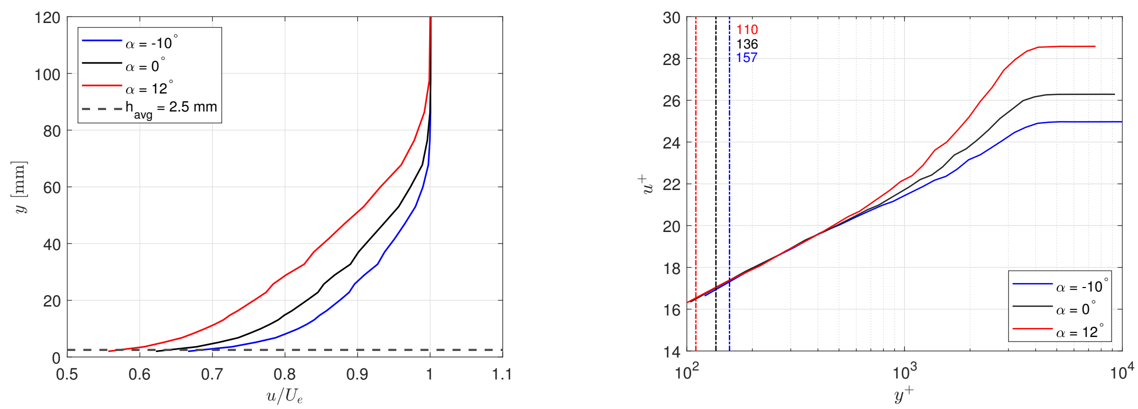

(a) Boundary layer profile along with the average distance of the upper edge of the PIV laser sheet from the port wall

(b) Boundary layer profile in terms of the wall units along with the respective location of the upper edge of the PIV laser sheet.

Fig. 5 Boundary layer profiles at x = 3.09 m for $Re_c = 1.2 \times 10^6$ for the APG (red), SPG (black) and FPG (blue) cases.

In Figure 5(a), the horizontal axis represents the streamwise velocity normalized with the edge velocity of the respective pressure gradient case, while the vertical axis shows the wall-normal distance in millimeters. The difference in the boundary layer thickness can be observed for the three pressure gradient cases here. A dashed black line shows the location of the upper edge of the laser sheet thickness used for wall parallel PIV measurements.

To get a perspective in terms of wall units, Figure 5(b) shows the boundary layer profile along with the average location of the laser sheet's upper edge. It is important to note that the friction velocity (u_τ) varies for the three pressure gradients. Since the wall-normal height of the laser sheet in terms of the wall units depends on friction velocity, it is different for the three different pressure gradients. Equation 3 shows the relation between the height of the laser sheet in terms of wall units and the distance of the laser sheet's upper edge to the wall.

$$h^+ = \frac{h u_\tau}{\nu} \tag{3}$$

The numerical results extracted from the boundary layer data are essential for the spectral analysis of the velocity fluctuations. The critical parameters used throughout this paper, along with their values, are shown in Table 1.

Parameters	Units	Case I	Case II	Case III
Airfoil Angle of Attack (α)	°	-10	0	12
Mean Pressure Gradient (dC_p/dx)	1/m	-0.143	-0.041	+0.074
Clauser pressure gradient parameter (β)		-0.292	-0.127	+0.409
Freestream Velocity (U_∞)	m/s	22.8	22.9	22.8
Edge Velocity (U_e)	m/s	26.0	23.6	20.9
Friction to Edge Velocity Ratio (u_τ/U_e)		0.040	0.038	0.035
Freestream Mach Number (Ma)		0.074	0.068	0.060
Boundary Layer Thickness (δ)	mm	58.7	67.5	83.6
Displacement Thickness (δ^*)	mm	6.6	9.0	13.5
Momentum Thickness (θ)	mm	5.3	7.0	10
Momentum Thickness Reynolds Number (Re_θ)		7.93×10^3	9.56×10^3	12.05×10^3
Friction Reynolds Number (Re_τ)		3.53×10^3	3.49×10^3	3.52×10^3
Viscous Length Scale (ν/u_τ)	mm	16.6×10^{-3}	19.3×10^{-3}	23.8×10^{-3}
Shape Factor (H)		1.25	1.28	1.35
Coefficient of Friction (C_f)		3.2×10^{-3}	2.9×10^{-3}	2.5×10^{-3}

Table 1 Boundary Layer Parameters of the three pressure gradients (angles of attacks) used in the analysis for $Re_c = 1.2 \times 10^6$ at x = 3.09 m

C. Particle Image Velocimetry

Flow visualization measurements were conducted at the mid-span location of the port side wall using a wall-parallel, flow-aligned planar PIV in the $x - z$ plane. Figure 6 shows the experimental setup for one of the flow measurements.

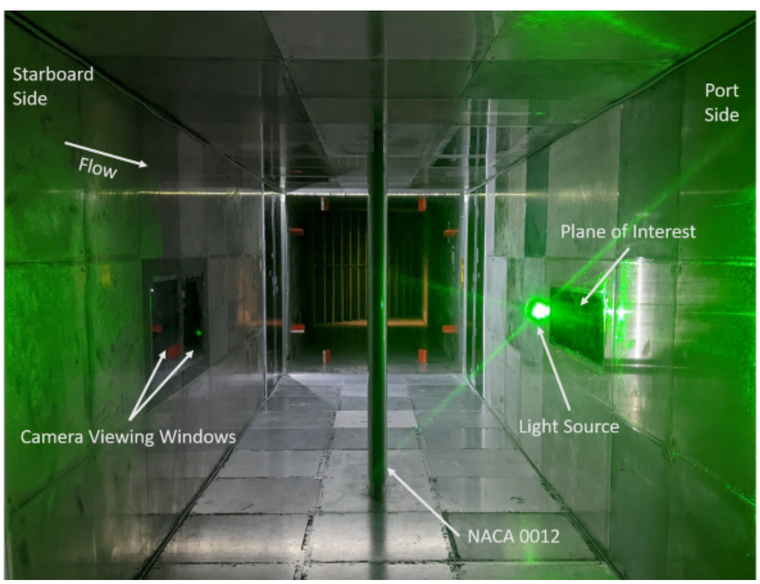

Fig. 6 Experimental setup for a PIV measurement (view from flow's perspective)

Two Phantom v2512 cameras were mounted on the starboard side such that their sensing surface faced the port wall of the test section, and their fields of view grazed a transparent acrylic window mounted on the port side wall. Both cameras used a Nikon AF-S Nikkor 200 mm lenses and were separated by 266.7 mm (lens' center-to-center distance) from one another. Figure 7 shows the two cameras mounted on the starboard side wall. In this figure, the upstream camera is labeled as Camera 1, while the downstream camera is labeled as Camera 2. This convention will be used throughout the paper.

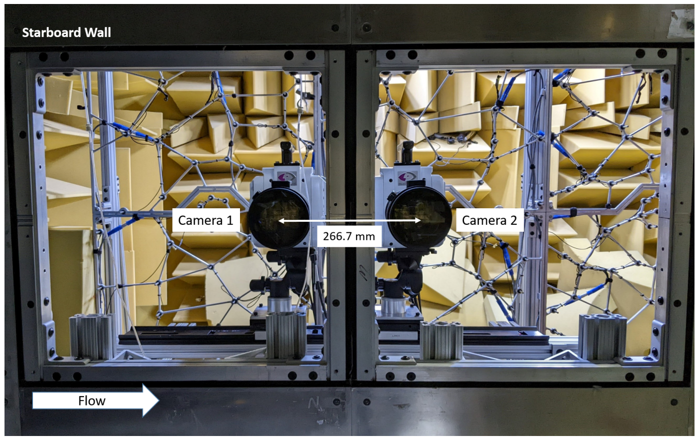

Fig. 7 Camera Setup showing the separation between the center of the lenses

Camera 1 operated at a working distance of 1.92 m and provided a field of view (FOV) of 333 mm in the streamwise direction and 206 mm in the spanwise direction. Camera 2 operated at a working distance of 1.91 m and provided a FOV of 329 mm × 206 mm. A streamwise overlap of 55 mm (9.2% of the combined FOV) was intentionally created between the fields of view of the respective cameras to allow a smooth merging of the flow field and an optical calibration using a single coordinate system. This provided an overall field of view of size 606 mm × 200 mm. A schematic of this procedure has been shown in Figure 8. Please note that the figure is not to scale, and the offset between the two frames has been greatly exaggerated for ease of understanding. In Figure 8, the blue area (along with the dimensions colored blue) represents the FOV of Camera 1, while Camera 2 is represented in the green area with its dimensions markers also shown in green. The overlapping area of both fields of view is shown as a dotted perimeter, along with its dimensions in black. The combined FOV is centered around the midpoint of the overlapping area (shown as a vertical black dashed line).

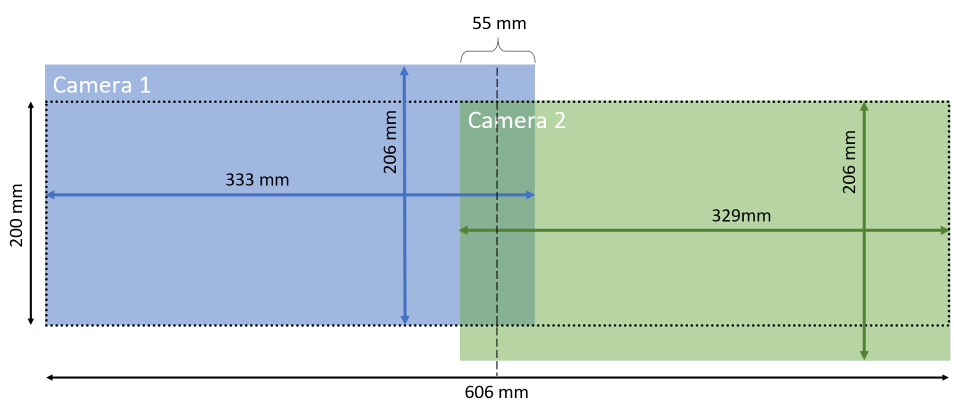

Fig. 8 Schematic of the fields of view of both cameras in overlapping planar configuration grazing the port wall

The data outside the black dotted parameter has not been used in any of the analyses presented in this paper. To allow a smooth merge between both fields of view, a hyperbolic tangent weighting function W, was applied to both fields of view. This removed any apparent sharp jumps between the velocity field at the point where the two fields of view connected. This function is given in Equation 4.

$$W = \frac{1}{2}\left[1 \pm \tanh\left(\frac{X_c - 0.3X}{X}\right)\right] \tag{4}$$

Here, X represents the streamwise FOV of each camera while the subscript c is placed for the midpoint of the horizontal (streamwise) FOV. The vector fields were multiplied with the weighting functions and then added to give a smoothly merged vector field.

The two acrylic windows mounted on the starboard wall (as shown in Figure 7) allowed the cameras to take images of the flow that was illuminated by a dual-pulsed 532 nm Nd:YaG laser on the port side wall. This laser was emitted by Photonics Industries DM series system and provided a total energy of 25 MJ per pulse. A plano-concave lens (focal length = -20 mm) was used to convert the laser beam into a thin sheet of laser (1-2 mm thick) that grazed the port wall. Since the laser sheet was required to cover a larger area ($\approx$ 600 mm $\times$ 200 mm), special attention was given to ensure that the laser sheet remained at a permanent grazing angle to the wall. This was achieved by adjusting the focal length of the laser collimator such that the two pulses of the laser sheet converged to a minimum thickness (i.e., 1.5 mm) near the upstream edge of the FOV. Within the merged field of view, the upper edge of the laser sheet remained between $y^+ \approx 120$ and $y^+ \approx 150$. The wall aluminum panels were replaced with a large transparent acrylic panel to minimize potential reflections from the surface. This provided confidence to make the laser sheet graze the wall at the smallest possible height. The test section was populated with propylene glycol particles (nominal diameter of 500-700 nm) generated using an MDG fog generator to illuminate the flow.

The PIV cameras were calibrated using a 2D calibration plate, designed in-house using an open-source tool. The calibration plate provided filled black circles as targets for the cameras. These circles were 10 mm in diameter and were arranged in a Cartesian grid configuration with a uniform spacing of 30 mm in either direction. A total of 494 circles were arranged in 19 rows and 26 columns over a 5.5 mm thick board, 800 mm $\times$ 600 mm in size. The calibration plate was installed on top of the transparent acrylic panel at the port wall, and the cameras were calibrated on the free surface of the plate. Once the cameras were calibrated, the calibration plate was removed, and the cameras and laser were traversed linearly by a distance equal to the thickness of the calibration plate (i.e., 5.5 mm) such that the laser sheet and the camera's field of view grazed the port wall. This traversing action was executed using a Parker 4422 linear mechanical traverse that provided a linear travel accuracy of 2 μm over a travel distance of 25 mm.

The laser sheet was introduced to the flow via a cutout in one of the panels downstream from the area of interest, where the collimator was mounted. To minimize any blockage effects caused by the presence of the laser collimator, this region was covered with a NACA 0032 fairing which was manufactured using rapid prototyping, to allow smooth un-separated flow to convect around the laser. Figure 9 shows the fairing that functioned as an aerodynamic housing for the laser head. A rectangular cutout of 38.1 mm $\times$ 12.7 mm cross-sectional area allows the laser to exit the fairing and illuminate the oncoming flow. This rectangular cutout was also sealed with a transparent acrylic window to prevent contamination from entering the fairing and influencing the laser lens.

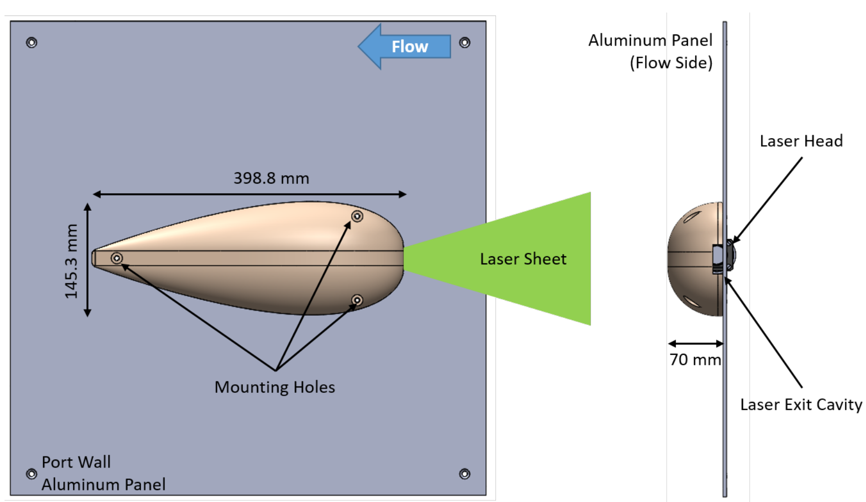

Fig. 9 Schematic of the NACA 0032 fairing to allow safe housing of the laser head with minimal aerodynamic blockage effects

The left side of Figure 9 shows a view of the port wall by an observer standing in the test section, while the right side of the figure shows a view from upstream of the fairing. Using ideal flow analysis, it was calculated that the laser fairing impacted the flow as far as 80 mm upstream of its leading edge, which remains well outside (further downstream) of the field of view. The aerodynamic profile of the fairing also allowed gentle flow reattachment once it passed over the laser fairing. The PIV results shown in Section IV show no evidence of flow disturbance that can be directly attributed to the laser fairing and therefore confirm the anticipated behavior.

Using the high speed cameras, images were taken at sampling rates between 3.1 kHz to 3.75 kHz (depending on the convection velocity) in dual-frame mode. The laser and cameras were synchronized using a Programmable Timing Unit (PTU), and the entire system was operated in DaVis 10.0, which is a commercial PIV software provided by LaVision. The same software was later used to process the raw data. A sliding background subtraction was applied to groups of 4 consecutive images to remove contamination caused by any dust particle that passed through the FOV. Mild laser diffusion effects were observed near the edges of the images, causing a steep loss in signal-to-noise ratio (SNR). To address this, a uniform rectangular mask was applied to all images for all flow conditions to uphold consistency in the processing scheme. The data was then processed using two initial passes of 1:1 square correlation windows, 64×64 pixels in size with a 50% overlap between consecutive windows. Then three additional passes of 1:1 circular correlation windows of size 32×32 pixels with 75% overlap were used. This processing scheme provided a spatial resolution of 8.40 mm. The generated vector fields were then imported and processed further using MATLAB.

IV. Results and Discussion

Data acquired using the setup described in Section III, and for the flow conditions defined in Section III.B is presented in this section. However, a brief overview of the pressure gradient effects on the boundary layer will be discussed before dissecting the results for further analysis.

A. Effects on mean velocity and the boundary layer

Boundary layer growth within the field of view was observed as a direct consequence of the wind-tunnel's overall favorable pressure gradient (even in the absence of a pressure-gradient generating airfoil). In other words, the mean flow velocity varied between the upstream and the downstream region of the measurement plane. This effect is visible in the time-average contours of the streamwise velocity, shown in Figure 10.

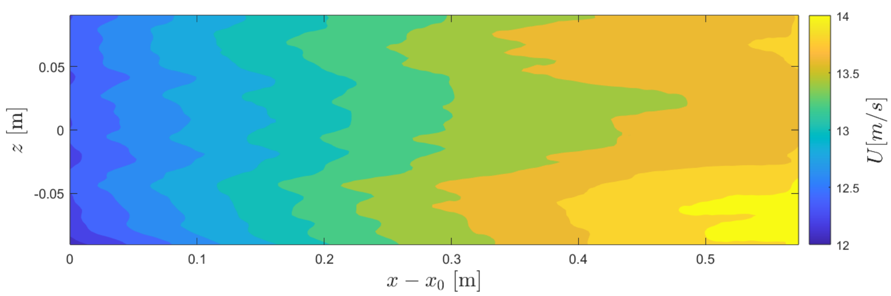

Fig. 10 Time-averaged streamwise velocity for the small pressure gradient (SPG) case

In Figure 10, the horizontal and vertical axes show the streamwise and spanwise distances in meters, while the contours show the time-averaged velocity for 48,000 time realizations taken as two separate sample sets (24,000 images per set). Averaging the velocity separately in the streamwise and spanwise direction for all pressure gradient cases reveals the mean pressure gradient effects. Figure 11a shows the spanwise-averaged streamwise velocity (U_c) as a function of the streamwise distance (x). The variation of the streamwise-averaged streamwise velocity U_s with spanwise distance (z) is shown in Figure 11b.

Figure 11 shows a general trend, indicating faster local mean velocities for the favorable pressure gradient (FPG) case (as high as 67% of the edge velocity). In contrast, the adverse pressure gradient indicates slower mean convection (as high as 53% of the edge velocity within the FOV). The increase in the convection velocity for the favorable pressure gradient is a direct consequence of the variation in the boundary layer parameters (δ, θ, U_e, etc.) within the field of view. In other words, while the measurement plane physically remained at a constant height from the smooth wall for all pressure-gradient cases, the variation in the boundary layer thickness caused the laser sheet to graze a different region of the boundary layer (in wall-units, see Figure 5), resulting in a different observed velocity within the plane of

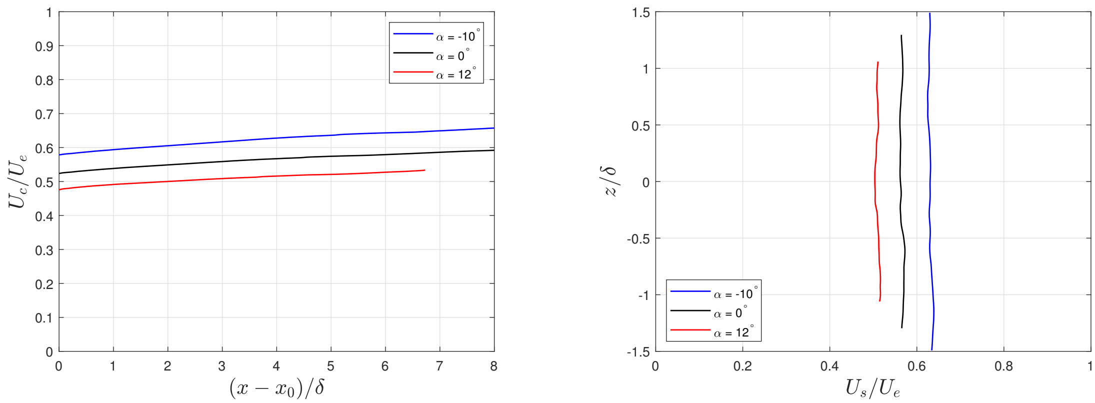

(a) Variation of the spanwise-averaged mean convection velocity with streamwise distance, normalized with the local boundary layer thickness

(b) Variation of the streamwise-averaged mean convection velocity with spanwise distance, normalized with the local boundary layer thickness

Fig. 11 Variation of the convection velocities within the FOV as a fraction of the local edge velocities.

measurement for each case. To confirm the boundary layer growth and the streamwise variation in δ, boundary layer profiles from three different streamwise stations were compared. Recall that the boundary layer data was acquired using a boundary layer rake mounted at the port wall's mid-span location ($z = 0$) at a streamwise distance of $x = 3.08$ m away from the origin. It is acknowledged that the boundary layer proceeds to vary beyond this point, and hence the parameters presented in Table 1 do not remain constant throughout the FOV. Therefore, the boundary layer parameters are linearly interpolated between the locations where data was acquired (i.e., between three streamwise stations at $x = 2.47$ m, 3.08 m, and 3.68 m). This allows local normalization of data with boundary layer parameters specific to each streamwise location within the FOV. Figure 12 shows the variation of the boundary layer thickness δ, with the streamwise distance x for the three pressure gradient cases.

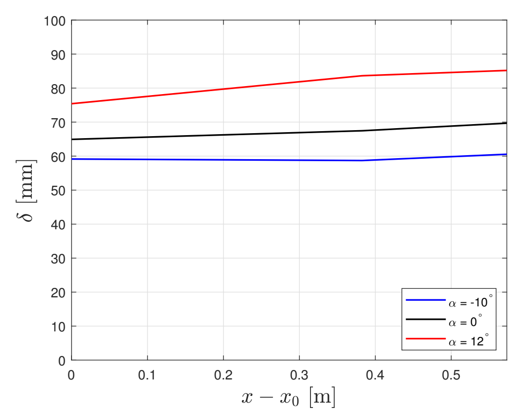

Fig. 12 Variation of boundary layer thickness, using linear interpolation between streamwise stations at x = 2.47, 3.08, 3.68 m.

The vertical axis in this figure corresponds to the boundary layer thickness (δ) in millimeters. As predicted, a general growth in the boundary layer thickness is observed as flow moves downstream due to the pressure gradient provided by the wind tunnel. However, the growth rate is higher for the APG case, while little to no growth is observed for the SPG and FPG cases. Similar results are obtained for other boundary layer parameters and therefore are not presented to avoid reiteration of the same phenomenon. Figure 12 provides a basis for normalization that will be followed for future analyses. Since the APG case corresponds to a thicker boundary layer, normalizing distances with δ will result in the apparent shrinking of physical quantities. The reverse is expected for the FPG case, where δ changes are comparatively minute.

The three pressure-gradients' mean-subtracted, streamwise velocity contours are shown for a particular time instance (t = 0s). The streamwise (horizontal) and the spanwise distance (vertical) have been normalized with the respective local boundary layer thickness for each of the three pressure-gradient cases. This results in inconsistent window sizes as three different values of δ are used for normalization. However, the physical size of the field of view remains the same (refer to Section III.C for the details regarding the field of view).

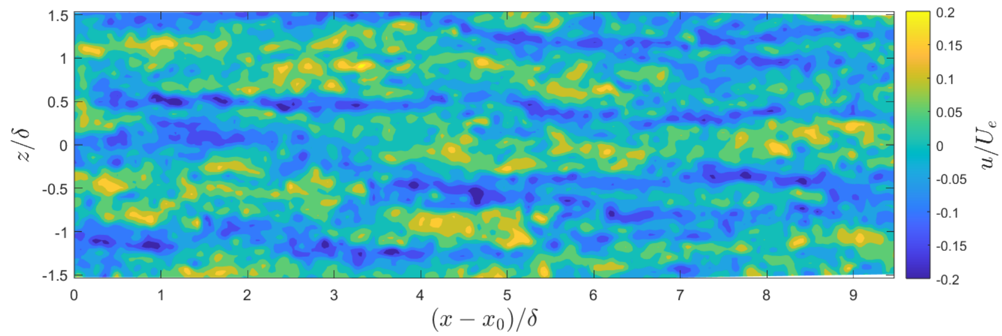

(a) Streamwise velocity contours for the favorable pressure gradient (FPG) case

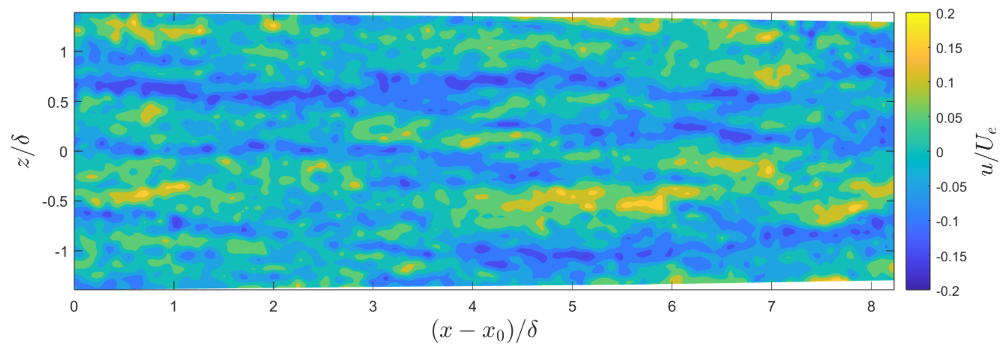

(b) Streamwise velocity contours for the near-zero pressure gradient (SPG) case

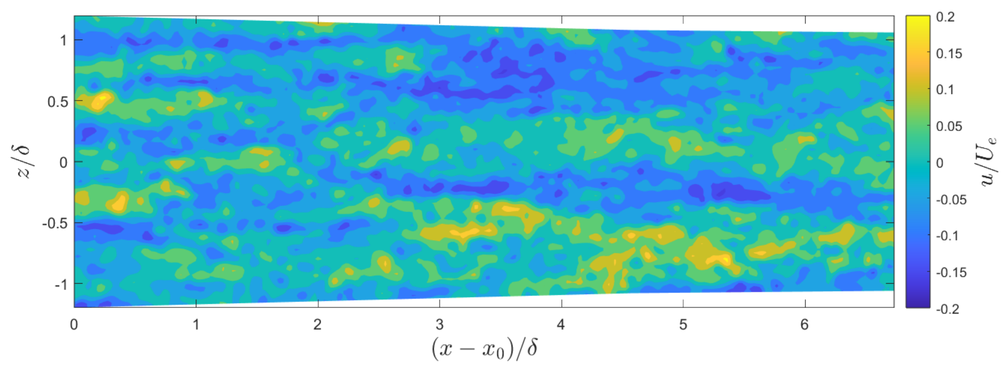

(c) Streamwise velocity contours for the adverse pressure gradient (APG) case

Fig. 13 Instantaneous, mean-subtracted streamwise velocity normalized with the edge velocity, at the first frame of the data acquired for each pressure gradient case

Several important conclusions can be drawn by comparing using the raw images for all three pressure-gradient cases.

First, the presence of long coherent structures, spread in the streamwise direction on the order of 10δ or greater, is evident from these raw images. These are the superstructures that were discussed to a great extent in Section II. The presence of high (yellow) and low (blue) momentum regions coexisting at the same wall-normal height is also evident, highlighting that a single value of the convection velocity to recreate velocity data remains a questionable approach beyond a certain streamwise distance. Consequently, this observation suggests that the validity of Taylor's frozen flow hypothesis over large streamwise distances must be carefully deliberated before drawing meaningful conclusions from the data.

A deeper look at the three velocity contours highlights the effects of pressure gradients. As the flow changes from adverse to a favorable pressure gradient (+12° to -10°), the width of the large structures decreases as they appear to get aligned in the streamwise direction. In other words, the favorable pressure gradients apply a virtual pull to these superstructures decreasing their spanwise spread and effectively aligning them along the streamwise direction. An expected variation in the length scales of the superstructures is expected, although detailed statistical analysis is required to unveil this trend more quantitatively. In addition to the spanwise spread, the long, slow-moving structures (shown as blue contours) also appear to be separated from one another by the relatively shorter ($\sim 1\delta$) but faster-moving structures. This separation appears smaller for the FPG case, allowing a higher number of slow-moving structures to fit within the spanwise FOV. In contrast, the opposite applies to the APG case, where the number of structures per area appears to be lower.

Another feature that must be clarified in the data set's first frame is the structure's meandering in the spanwise direction . The long structures meander downstream within the FOV at their local convection velocities (generally lower than the mean convection velocity). This gives them a snake-like slithering motion. This motion appears exaggerated for the APG cases, whereas the meandering gets diminished for the FPG case. Statistical tools, such as spatial and temporal correlations, will be used to establish quantitative behavior for the large-scale structures discussed.

B. Turbulence Statistics

In order to get a comparison of the turbulent statistics, the Reynolds stresses for the three pressure-gradients are compared. Table 2 shows the minimum, maximum, and average values of the streamwise, spanwise, and shear stresses. All the values presented in the table are normalized with the square of the local edge velocities.

	FPG		**SPG**		**APG**	
Parameters	**mean**	**variance**	**mean**	**variance**	**mean**	**variance**
$\overline{uu}/U_e^2$	4.49×10^{-3}	2.51×10^{-8}	4.29×10^{-3}	2.45×10^{-8}	5.04×10^{-3}	1.74×10^{-8}
$\overline{ww}/U_e^2$	1.54×10^{-3}	1.84×10^{-8}	1.45×10^{-3}	1.19×10^{-8}	1.80×10^{-3}	9.83×10^{-9}
$\overline{uw}/U_e^2$	7.52×10^{-5}	6.35×10^{-9}	9.78×10^{-5}	1.29×10^{-8}	8.43×10^{-5}	1.08×10^{-8}

Table 2 Variation of the Reynolds stresses (normalized with the local edge velocities) for the three pressure-gradient cases

The effects of insufficient spanwise resolution are unveiled by comparing the average values of the streamwise and spanwise Reynolds stresses. It can be seen that the streamwise Reynolds stress is about 3.0 times the spanwise Reynolds stress for the FPG and SPG cases, while this ratio drops to 2.8 for the APG case. Established data presented in [26] and [27] shows that for a smooth-wall turbulent boundary layer, the value of the spanwise Reynolds stress is generally on the order of the streamwise Reynolds stress, and not a third of its value as shown in Table 2. Since the study aimed explicitly for streamwise aligned large-scale coherent structures, giving up the spatial resolution to capture a large FOV was a deliberate experimental decision. Therefore, the under-resolution of the data in both the streamwise and spanwise distance is possibly a consequence of such a trade-off. This attenuation of streamwise and spanwise Reynolds stresses has been observed in both smooth-wall [28] and in rough-walls [29]. Nevertheless, the average values, at their respective wall-normal heights can be compared to the wall-normal PIV data acquired at the same flow conditions by Vishwanathan et. al. [30]. Figure 14 compares the wall-normal and wall-parallel data for the streamwise Reynolds stresses. Please note that no wall-normal data is provided for the spanwise Reynolds stresses, and it is only presented to make relative comparisons with the streamwise Reynolds stresses.

The horizontal axis in this figure corresponds to wall-normal distance normalized with the boundary layer thickness, while the vertical axis corresponds to the streamwise Reynolds stress component. The solid lines represent the streamwise

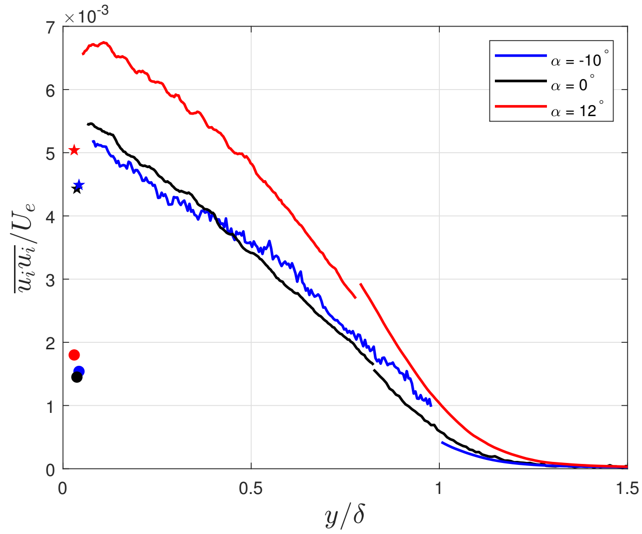

Fig. 14 Comparison of the measured streamwise (filled pentagrams) and spanwise Reynolds stresses (filled circles) with wall-normal PIV data by Vishwanathan et. al. [30] (solid lines).

Reynolds stresses acquired from the wall-normal PIV measurement, while the filled pentagrams represent the data (spatially averaged over the entire FOV) from the wall-parallel PIV measurements. In addition to the stream Reynolds stresses, the spanwise Reynolds stresses are plotted on the same plot as filled circles. The location of this data in terms of the wall-normal distance has also been normalized with the boundary layer thickness and corresponds to the average height of the laser sheet's upper edge throughout the FOV. The color scheme is kept consistent with the previous figures, as discussed earlier. Figure 14 shows that the wall-normal data failed to resolve the statistics closer to the wall where the wall-parallel data was acquired. It is important to note that while the wall-parallel configuration provided access to near-wall domain, it also averaged the data within the thickness of the laser sheet.

As discussed previously, a quantitative analysis to unveil the spatial information of the structures was conducted using spatial anchored correlation coefficients (ρ_{uu}). Several anchor points (points that were correlated with all other points within the FOV for all time instances) were used. However, only the anchor point roughly in the center of the FOV ($x = 0.3$ m, $z = 0$ m) is presented here. Figure 15 show the correlation coefficients for the selected anchor point. The positively correlated regions are shown as light shades of yellow, while the negatively correlated regions are shown using darker shades of blue.

A streamwise aligned region of highly correlated flow is seen around the anchor point, confirming the presence of coherence along the streamwise direction. Of course, as we move away from the anchor point in either direction, the correlation decays away. It is important to note that this does not mean that the edges of these correlations represent the length scales of the coherent motions present within the flow. In fact, the length scales represented using streamwise correlation coefficients are restricted due to the limited size of the FOV. In other words, the restriction of the streamwise extent of the FOV limits us to a separation $\Delta x \approx 0.27$ m in either a positive or negative streamwise direction. That being said, the effects of the pressure gradients on these correlation contours are still evident. It can be seen that as the pressure-gradient varies from favorable to adverse (top to bottom in Figure 15), the streamwise and spanwise spread of the correlated region increases. For a value of $\rho_{uu} = 0.1$, the streamwise extent of the correlation spans about 0.365 m, whereas this spread increases to 0.399 m for the SPG case and 0.456 m for the APG case. The value for the spanwise spread of this correlation coefficient is 0.021 m, 0.025 m, 0.034 m for the FPG, SPG and the APG case, respectively, increasing as the mean pressure-gradient varies from favorable to an adverse pressure gradient. This also confirms the enhanced streamwise spread of the structures observed in the raw snapshots of the APG cases (Figure 13). An interesting observation is made while comparing the contour lines' spanwise spread at a particular correlation coefficient value. It is observed that the correlated regions around the anchor point show spanwise symmetry, i.e., the edges of the correlated regions are equidistant from the anchor point in the positive and negative spanwise separation. This trend is not seen for the APG case, where the correlated regions show a lack of spanwise symmetry about the mid-span location of the FOV. This may be an indication of relatively increased meandering behavior for the APG case.

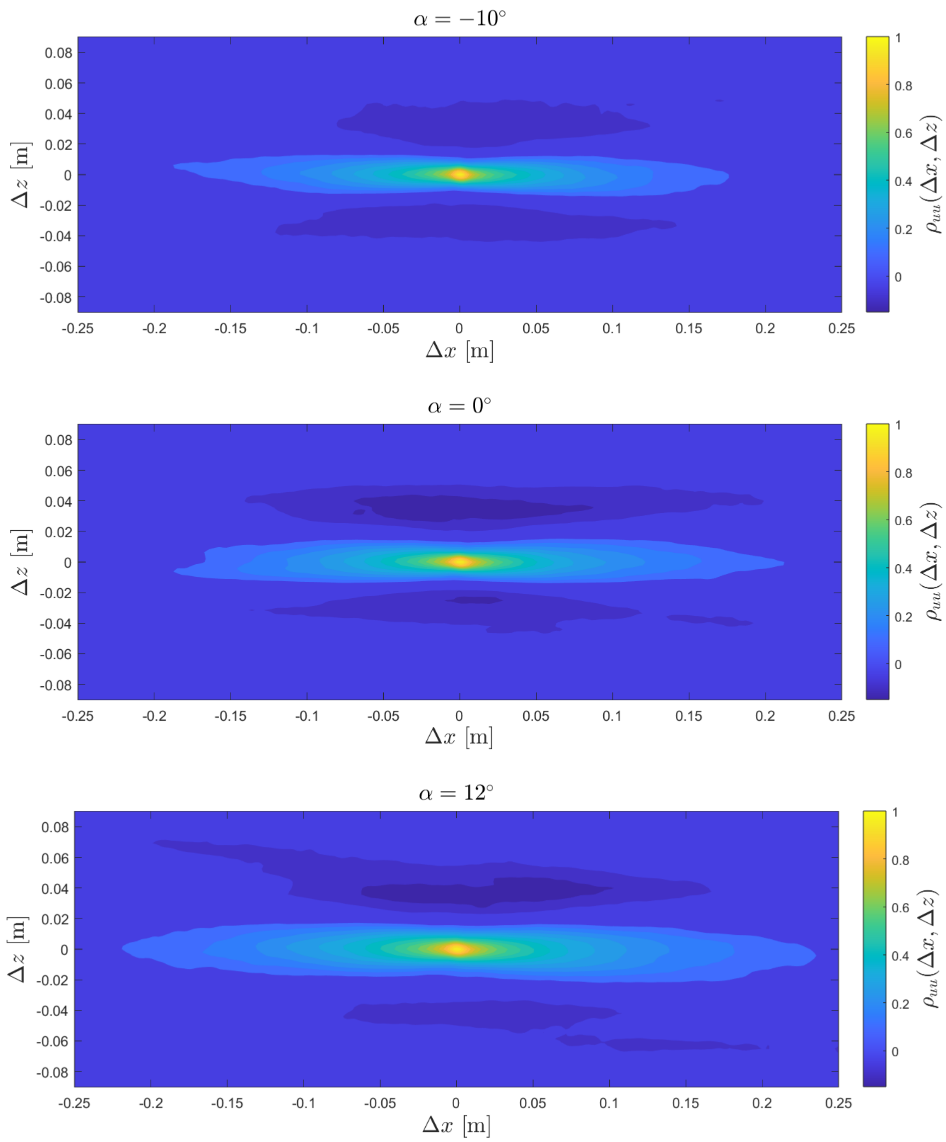

Fig. 15 Correlation coefficient of the streamwise velocity at the anchor point (x, z) = (0.3, 0) m for the three pressure gradient cases: FPG (top), SPG (middle) and APG (bottom).

A similar trend is observed in the spanwise separation between the negatively correlated regions (shown as dark shades in Figure 15). These negatively correlated regions (with the anchor-point) get further apart for the APG case compared to the FPG cases, suggesting loosely stacked positive and negative structures within the FOV (refer to the discussion regarding Figure 13).

For a direct comparison, the data presented in Figure 15 is normalized using the respective streamwise averaged-boundary layer thickness for each of the three pressure-gradient and their contours are superimposed on a single plot. Figure 16 allows quantitative comparison by plotting contours for a few selected levels (i.e., ρ_{uu} = -0.07, 0.1, 0.8). Here the negative correlations are shown as dashed lines, while the positive correlated levels are shown as solid lines. The color schemes are kept consistent with the previous figures.

Normalizing the domain using δ_{avg} for the respective pressure-gradient case allows the correlation contours to collapse on one another. The extent of the correlation $\rho_{uu} = 0.1$ covers a region roughly equal to 6δ in the streamwise and 0.42δ in the spanwise direction. Correlated regions beyond this value cover a larger extent of the FOV, but they are not shown to avoid confusion regarding their edges. The negatively correlated regions show a relatively weaker collapse,

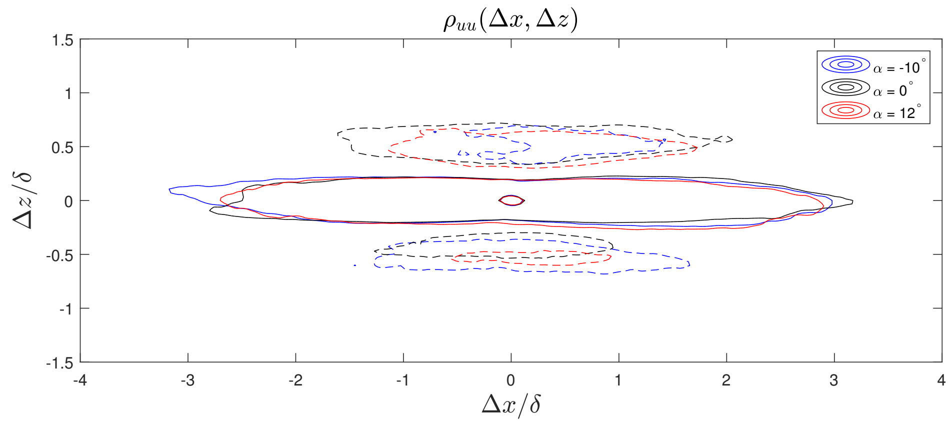

Fig. 16 Comparison of the extent of the streamwise velocity correlations for the three pressure-gradient cases for ρ_{uu} = 0.8, 0.1 (solid lines) and ρ_{uu} = -0.07 (dashed lines)

especially in the negative spanwise direction. Admittedly, this behavior needs to be explored quantitatively in more depth.

For the SPG case, a slice of the spatial correlations calculated at various spanwise and streamwise points within the FOV is shown in Figure 17. The purpose of showing these results is to establish the extent of streamwise and spanwise flow homogeneity within the bounds of our planar domain. Five different points in the streamwise and spanwise are held as anchors separately. The solid lines represent the values for the streamwise velocity fluctuations (u), while the dashed lines represent the spanwise velocity fluctuations (w).

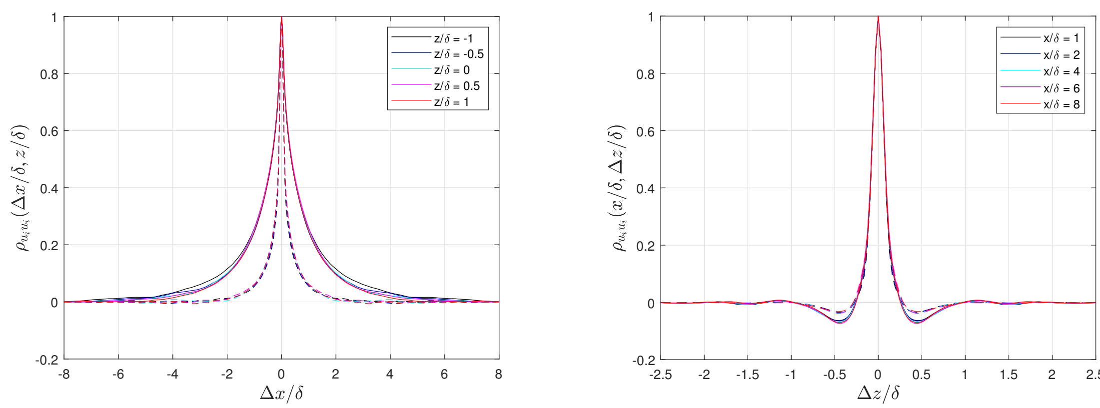

(a) Correlation coefficient of the streamwise and spanwise velocity as a function of streamwise distance (as observed from 5 spanwise anchor points)

(b) Correlation coefficient of the streamwise and spanwise velocity as a function of spanwise distance (as observed from 5 streamwise anchor points)

Fig. 17 Variation of the streamwise velocity correlation within the field of view for ten different anchor points for the SPG case. Solid lines represent streamwise velocity, while dashed lines represent the spanwise velocity.

As expected, the spanwise velocity predicts small length scales, supported by the width of the correlation curve. In other words, as flow convects downstream, the correlation in the spanwise velocity fluctuations decays much faster when compared to the streamwise velocity. This difference in the decay rate between the u and w velocities is not observed in the spanwise direction, and a neat collapse is observed in this direction. The spatial correlations calculated at five different streamwise and spanwise points collapse on one another, suggesting the presence of spanwise and streamwise homogeneity in the boundary layer. To highlight these trends as a function of the mean pressure gradients, the anchor points at $(x, z) = (4, 0)\delta$ are selected for comparison in Figure 18.

Interestingly, the collapsing of the ρ_{uu} and ρ_{ww} curves, as shown in Figure 17, is repeated. The extent where the

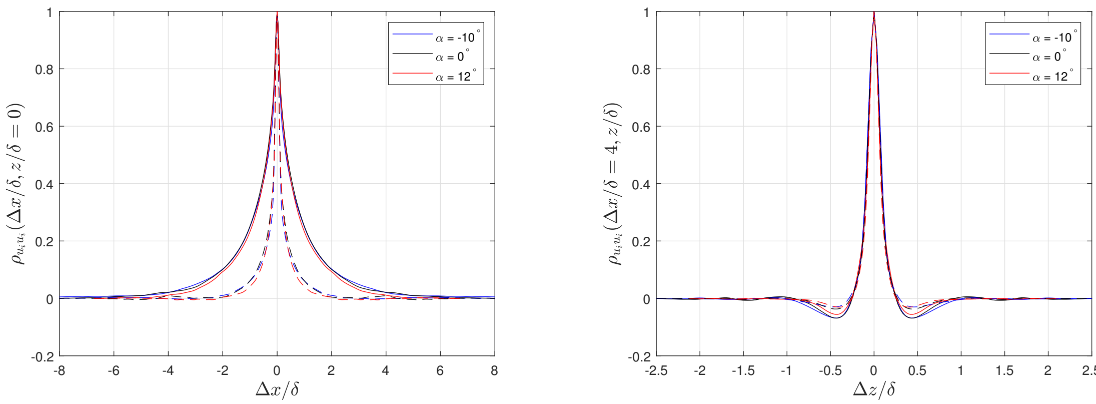

(a) Correlation coefficient of the streamwise and spanwise velocity as a function of streamwise distance

(b) Correlation coefficient of the streamwise and spanwise velocity as a function of spanwise distance

Fig. 18 Variation of the streamwise velocity correlation coefficient as a function of mean pressure-gradient. Solid lines represent streamwise velocity, while dashed lines represent the spanwise velocity.

streamwise velocity correlation remains a non-zero value spans throughout the FOV (i.e., $6 - 8\delta$ depending on the pressure-gradient case). This advocates for presence of streamwise-oriented structures that are much larger than the existing FOV. The faster decay in the spanwise correlation also confirms the flow anisotropy within the measurement plane. The spatial correlation functions also allow the estimation of integral length scales using Equation 5.

$$L_{ij} = \int_0^\infty \rho_{u_i u_i}(\Delta x_i) d\Delta x_i \tag{5}$$

For a finite domain size, the integral is evaluated between the edges of the domains, i.e., from $x = x_0$ m to $x = x_0 + 0.57$ m and $z = -0.09$ m to $z = 0.09$ m. The spanwise integral length scales (L_{13}, L_{33}) are shown in Figure 19(a) while the streamwise integral length scales (L_{11}, L_{31}) are shown in Figure 19(b). For ease of visualization, the horizontal axis represents the streamwise distance and streamwise-oriented length scales, while the vertical axis represents the spanwise direction and the spanwise-oriented length scales.

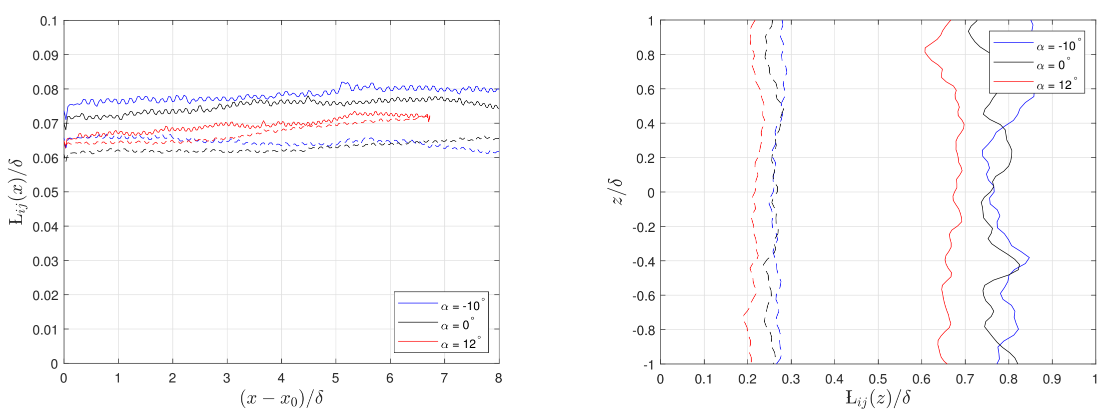

(a) L_{33}: solid lines, L_{13}: dashed lines

(b) L_{11}: solid lines, L_{31}: dashed lines

Fig. 19 Integral Length scales of the streamwise and spanwise velocities

The streamwise integral length scales of the streamwise velocity (L_{11}) dominate as they are on the order of 1δ (between 65-85% of the boundary layer thickness), whereas L_{31} are on the order of 20-25% of δ. Comparatively, the integral length scales in the spanwise direction remain significantly low (between 6-8% of δ). The details are shown in Table 3 below.

	FPG		SPG		APG	
Length-scale	**mean**	**variance**	**mean**	**variance**	**mean**	**variance**
L_{11}/δ	0.80	1.3×10^{-3}	0.78	1.2×10^{-3}	0.67	4.3×10^{-4}
L_{31}/δ	0.27	2.1×10^{-4}	0.26	1.1×10^{-4}	0.22	1.2×10^{-4}
L_{13}/δ	0.06	1.9×10^{-6}	0.06	7.2×10^{-6}	0.07	2.6×10^{-5}
L_{33}/δ	0.08	2.9×10^{-6}	0.08	9.1×10^{-6}	0.07	2.2×10^{-5}

Table 3 Statistical distribution of the length-scales within the measurement plane for the three pressure gradient cases

The flow's streamwise dominant anisotropic nature is again evident from Figure 19 and Table 3. As expected, the streamwise oriented integral length scales normalized with the boundary layer thickness are an order of magnitude greater for all pressure-gradient cases when compared with those in the spanwise direction. On the other hand, the length scales oriented in the spanwise direction remain approximately the same for the three cases. The results in Figure 16 also support these trends.

C. Wavenumber-frequency spectra

As discussed earlier, the wavenumber-frequency spectra of the velocity fluctuations (ϕ_{uu}) decompose the velocity signal into its spatial and temporal components. The importance of such a 2-dimensional spectrum has been well established in the pressure measurements presented earlier in [9] and [10]. However, the generation of wall-pressure fluctuations in a smooth surface can only be wholly explained by understanding the turbulence that induces these pressure fluctuations. Analogous to Equation 1, the wavenumber-spectrum of the velocity fluctuations can be calculated at a specific spanwise station within the planar field of view.

$$\phi_{uu}(k_x, z, \omega) = \frac{1}{(2\pi)^2} \int_{-R_\infty}^{+R_\infty} \int_{-T_\infty}^{+T_\infty} R_{uu}(\Delta x, \tau) e^{-i(k_x.\Delta x - \omega t)}\, d\tau dx \tag{6}$$

For a direct comparison, the spanwise location is selected to be the same location where the low-wavenumber pressure array was mounted, i.e., $z = 0$ m (refer to the experimental setup described in [10]). The spanwise location is kept consistent for the analysis and is shown as z_0 in the results. It is important to note that although the pressure and velocity measurements were taken at the same physical location in the test section, they were not taken synchronously. Moreover, the sampling frequency and spatial resolution of the two measurement modes differed. For instance, the wall-pressure fluctuations for the SPG case were sampled at 65.536 kHz, while the velocity signal was sampled at 3.75 kHz. The total sampling time also varied for the two measurements. While the pressure was sampled for 32 seconds, the velocity data was only taken for 6.4 seconds for each data set. These parameters directly impact the wavenumber and frequency range and resolution presented in the analysis. Since the velocity measurements were sampled with a relatively higher spatial resolution than the pressure measurements, the velocity spectra could resolve a more extensive range of wavenumber. The opposite is true for the frequency component (i.e., the pressure measurements were resolved for a more extensive range of frequencies). For the pressure measurements, the wavenumber resolution is 6.5 rad/m, while the frequency resolution is 50.3 rad/s. Similarly, for the velocity measurements, the wavenumber resolution is 11.0 rad/m, while the frequency resolution is 184.1 rad/s (SPG) and 152.2 rad/s (FPG and APG). Nevertheless, the plots presented in Figures 20 - 22 compare the streamwise wavenumber-frequency spectra of the streamwise velocity (left) with the surface pressure fluctuations (right). The data are presented for a normalized frequency range $\omega\delta^*/U_e = 4.5$ for easier comparison. Wavenumbers (presented on the horizontal axis) and frequencies (vertical axis) are normalized with the boundary layer parameters, specifically the displacement thickness δ^*, and the boundary layer edge velocity U_e. This normalization is kept consistent throughout the discussion as well.

Figure 20 shows the streamwise wavenumber-frequency spectra of the pressure and velocity fluctuations for the FPG case. The $x-$axis shows the wavenumber normalized on the displacement thickness, and the $y-$axis shows the frequency normalized on displacement thickness and the edge velocity of the boundary layer. It is important to note

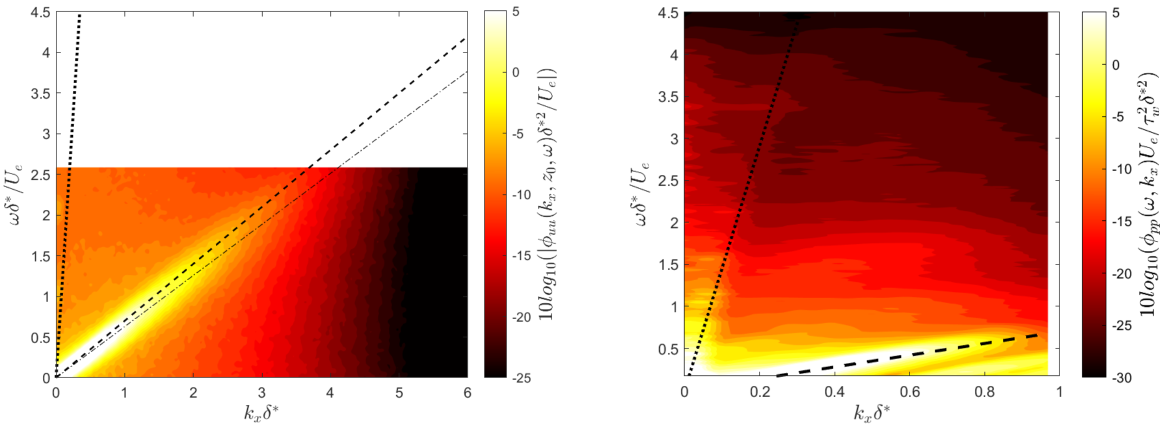

(a) Wavenumber-frequency spectrum of streamwise velocity fluctuations (b) Wavenumber-frequency spectrum of wall-pressure fluctuations

Fig. 20 Comparison of the streamwise wavenumber-frequency spectrum of the velocity (left) and the pressure (right) fluctuations for the FPG case at the midspan location.

that the two plots show different quantities. However, the degree of association is high, reflecting the characteristics of large-scale structures in the velocity field to pressure fluctuations. Figure 20(a) shows the velocity spectrum at a specific spanwise location in the field of view, whereas Figure 20(b) shows the near zero-spanwise separation or spanwise averaged normalized pressure spectrum due to the finite spanwise separation between the two rows of sensors. The spanwise location chosen for the velocity spectrum corresponds to the location of the array of sensors in the field of view. Due to the limited range of normalized frequencies that were resolved by the measurements, the results are restricted to $\omega\delta^*/U_e = 2.6$ for this specific case. This restriction can be attributed to the choice of normalization, as the value of δ^* is relatively small. At the same time, the U_e is accelerated for the FPG case compared to the other cases, limiting the normalized frequency range.

Several essential features must be introduced here. The acoustic line (a slice of the acoustic cone as shown in Figure 1 taken at the $z = 0$ plane) is shown as a steep dotted line. This line's slope represents the sound speed calculated for the specific experimental conditions. While this feature may appear relatively uneventful in the velocity spectra, the pressure measurements show successful identification of the acoustic cone. In other words, the pressure events occurring at or above the speed of sound are captured within the acoustic line successfully.

High spectral levels are observed in pressure and velocity spectra which are concentrated at an angle. This dominant region is the convective ridge. Here it is essential to distinguish between the convective ridge shown in the pressure spectra and that shown in the velocity spectra. To understand this region in the pressure spectrum, a solid, dashed line is plotted at the convection velocity, the slope of which is assumed to be roughly 70% of the average edge velocity within the field of view. A corresponding solid-dashed line (with the same slope i.e., $0.7U_e$) is drawn on the velocity spectrum. Interestingly, the dominant region of the velocity spectrum is not distributed about this line. This is due to the fact that measurements were acquired at a specific height y from the wall, and therefore the plane of measurement only contains velocity data present within that slice of the boundary layer. Figure 5(b) shows the wall-normal height of these measurement locations. On the other hand, pressure being a global property, registers the effects of the entire boundary layer, not just a single slice. A dotted-dashed line is superimposed to understand the dominant region, *allegedly the convective ridge*, presented in the velocity spectrum. The slope of this line is the average velocity within the field of view, normalized with the edge velocity. As evident from Figure 20, the flow convective ridge appears to have a slope slightly lower than that of the pressure convective ridge. Another essential feature of the velocity spectra, highlighted by the convective line, is the separation of scales. At low wavenumbers, the convective ridge's slope closely matches that of the dotted-dashed line. However, the trend deviates at higher wavenumbers, suggesting the presence of fast-moving but relatively smaller-scale structures within the boundary layer. Nevertheless, the convective ridge remains the most dominant feature of the wavenumber-frequency spectrum.

A similar comparison is performed for the SPG case in Figure 21. The normalization and the line styles presented in Figure 21 are consistent with the previous figure. The trends observed in the convective ridge are also repeated here,

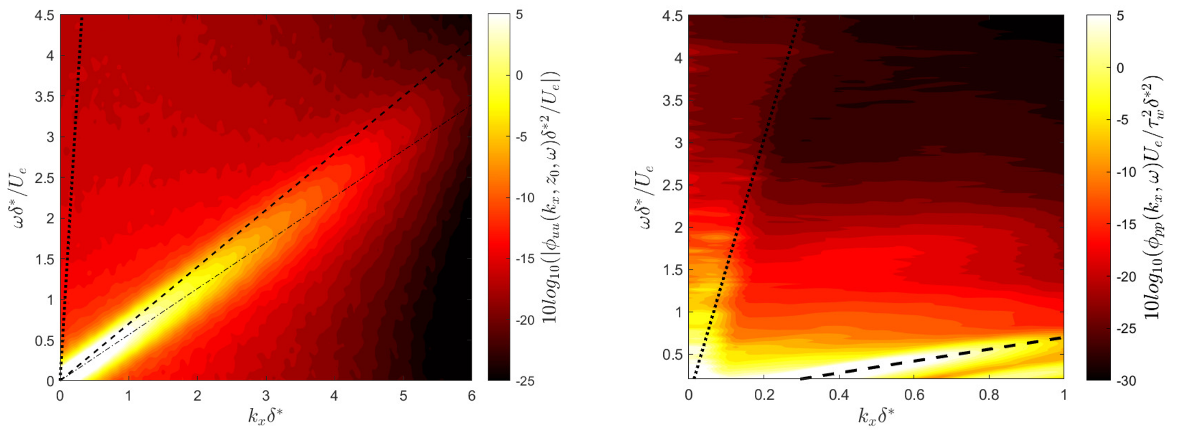

(a) Wavenumber-frequency spectrum of streamwise velocity fluctuations (b) Wavenumber-frequency spectrum of wall-pressure fluctuations

Fig. 21 Comparison of the streamwise wavenumber-frequency spectrum of the velocity (left) and the pressure (right) fluctuations for the SPG case at the midspan location.

including the deviation of the spectral levels towards increased frequency at high wavenumbers. At a fixed normalized frequency of 1.9, the spectral levels drop by 6.7 dB by moving two normalized wavenumber units in the subconvective direction (i.e., from 3 to 1). In contrast, the levels drop by 12.6 dB in the super-convective direction. Figure 22 shows the same trends for the APG case.

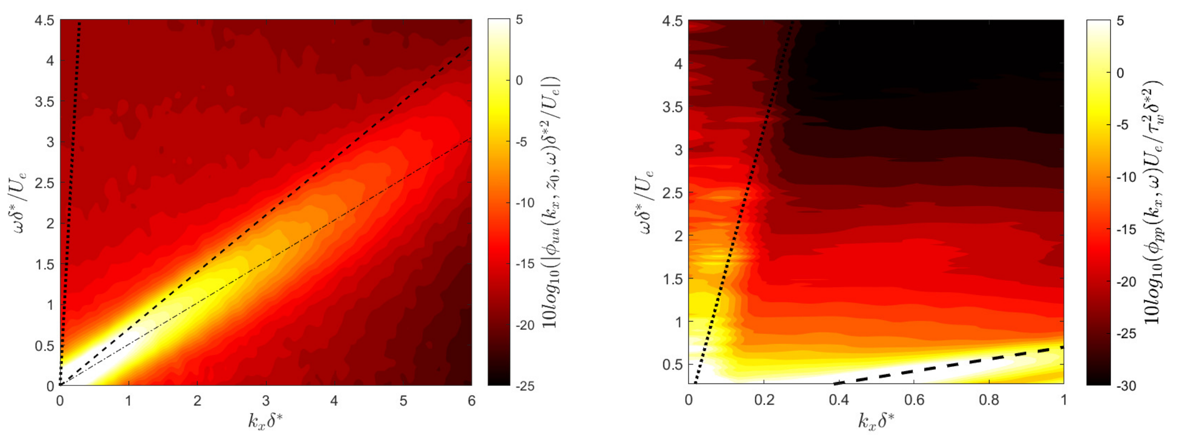

(a) Wavenumber-frequency spectrum of streamwise velocity fluctuations (b) Wavenumber-frequency spectrum of wall-pressure fluctuations

Fig. 22 Comparison of the streamwise wavenumber-frequency spectrum of velocity and pressure fluctuations for the APG case at the midspan location.

From the figures presented above, it can be seen that both the pressure and velocity spectra show an asymmetrical distribution of spectral levels about the convective ridge, which is biased heavily to the subconvective wavenumbers. Out of the three pressure gradient cases, the favorable pressure gradient cases show elevated levels at the subconvective regions for both the pressure and velocity spectra. This suggests the presence of large-scale turbulence with high-frequency content within the boundary layer. In other words, within the plane of measurement, the presence of large-scale structures that move rapidly across the FOV is suggested by the biased subconvective region.

Another way of understanding these effects is by comparing the levels at a fixed wavenumber. Figure 23 shows the normalized wavenumber-frequency spectra of the velocity and pressure fluctuations for a fixed normalized streamwise wavenumber, $k_x\delta = 0.4$. This number is selected to allow a direct comparison with the results provided earlier in [10].

Since a detailed discussion on the pressure spectra is presented in [10], the discussion here will focus more on the velocity spectra.

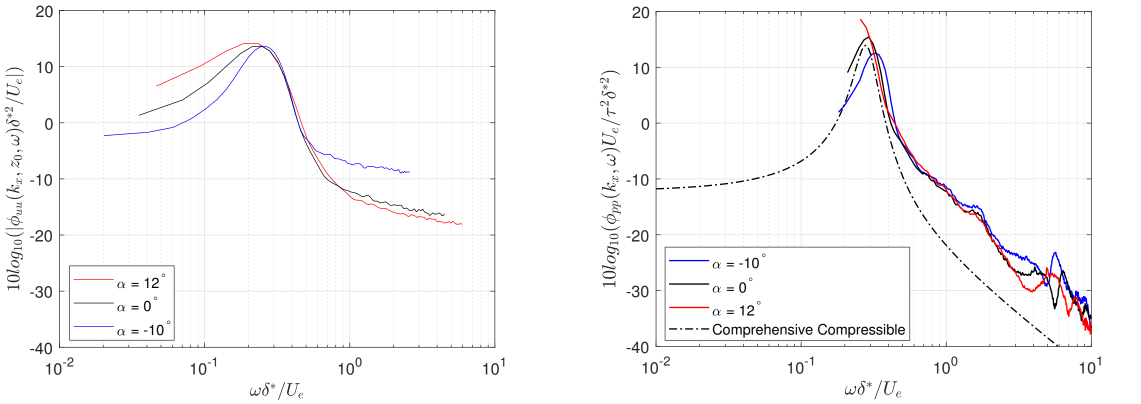

(a) Wavenumber-frequency spectrum of streamwise velocity fluctuations

(b) Wavenumber-frequency spectrum of wall-pressure fluctuations [10]

Fig. 23 Comparison of the streamwise wavenumber-frequency spectrum of the velocity (left) and the pressure (right) fluctuations with the comprehensive Chase spectrum [6] at $k_x\delta^*$ = 0.4.

In Figure 23, the horizontal axis shows normalized angular frequency, while the vertical axis represents the spectral levels. Note that the pressure spectra are normalized with the wall-shear τ_w to make the units compatible. A black dotted-dashed line is superimposed on the pressure spectra representing the Chase model at the experimental boundary layer parameters. A collapse is observed for the pressure spectra at and above the convective frequencies (the frequency at which the convective ridge occurs i.e, $\geq \omega\delta^*/U_e = 0.28$ for this case). This collapse lasts till a normalized frequency of 2.2 for the pressure but only till 0.57 for the velocity fluctuations. The peaks of the velocity spectra for the three pressure gradients also occur at different frequencies. The FPG case reaches a maximum of 13.6 dB at a normalized frequency of 0.26, while the SPG case peaks at the same level but at a slightly lower frequency of 0.23. The APG case shows a relatively higher peak of 14.1 dB at about $\omega\delta^*/U_e = 0.21$.

Another important observation is the width of the convective ridge, which varies for the three pressure gradient cases at the convective frequencies for both the velocity and pressure spectra. The poor resolution at lower frequencies for the APG case in the pressure spectra makes it challenging to quantify the width. However, the velocity spectra remain resolved at relatively lower frequencies as well. Clearly, for the APG case, the convective ridge appears to span a larger range of frequencies, when compared with the FPG case, while the SPG case remains sandwiched between them. This suggests that the APG case carries a wide range of frequency content around the convective ridge, a trend that can also be predicted by the near-wall Reynolds stresses (Figure 14 and Table 2). Interestingly, the convective ridge lasts for a much narrower range of frequencies for the pressure spectra compared to the velocity spectra.

This trend is flipped for the normalized frequencies higher than the convective frequency, at least for the velocity fluctuations, where the FPG case shows clear dominance compared to the other two cases. This suggests the dominance of high-frequency turbulence in the subconvective regime for the FPG case. At first glance, a similarity between the location of the spectral peaks and their levels is observed. Admittedly, the comparison between the pressure and velocity spectra at the selected wavenumber in Figure 23 creates the illusion that the parameters presented qualify for a direct comparison. Therefore, it is vital to distinguish between these plots and their interpretation. The similarities in their energy levels and the locations at which they peak must not be assumed to show a direct relation. That being said, the relation between the low-wavenumber pressure fluctuations and their sources cannot be discounted and must be investigated further.

D. Analysis with ResDMD

This section outlines how residual dynamic mode decomposition (ResDMD) [24, 25] can be applied to analyze the experimental data measured using wall parallel PIV to deduce essential flow features, specifically for studying the effects of different pressure gradients on wall-bounded turbulent flow. Using the notation from [24, 25], the data is viewed as snapshots $\mathbf{x}_n \in \Omega$ from a discrete dynamical system F such that

$$\mathbf{x}_{n+1} = F(\mathbf{x}_n), \quad n \geq 0. \tag{7}$$

The subscript n denotes a time step. The Koopman operator $\mathcal{K}$ acts on an 'observable' g, which is a function on the statespace Ω. For example, one can consider the data points as all the velocity-related information at some given timestep t_n. The observable g can also be considered a more specific subset of this data. For this study, the streamwise velocity of turbulence is of particular interest and hence can take g as the streamwise velocity at a timestep t_n. One can now define the Koopman operator $\mathcal{K}$ as the operator acting on g satisfying

$$[\mathcal{K}g]\,(\mathbf{x}_n) = g\,(F(\mathbf{x}_n)) = g(\mathbf{x}_{n+1}). \tag{8}$$

A particular advantage is that $\mathcal{K}$ will always be linear, regardless of the properties of the governing system being studied - see the review [31]. Thus, the time evolution of the system can be understood if an approximation for $\mathcal{K}$ and its spectral properties can be obtained. The catch is that $\mathcal{K}$ acts on an infinite-dimensional function space, meaning that computing its spectral properties can be a considerable challenge [23]. Challenges include spurious (unphysical) modes and dealing with continuous spectra, which both occur regularly in turbulent flows. ResDMD [24] overcomes such challenges through the data-driven computation of residuals associated with the full infinite-dimensional Koopman operator. ResDMD computes spectra and pseudospectra of general Koopman operators with error control and computes smoothed approximations of spectral measures (including continuous spectra) with explicit high-order convergence theorems. Several applications in various fluid dynamic situations at varying Reynolds numbers from both numerical and experimental data are given in [25]. Advantages of ResDMD include: the ability to resolve nonlinear and transient modes verifiably; the verification of learned choices of observables; the verification of Koopman mode decompositions; and spectral calculations with reduced broadening effects. The spectral properties of $\mathcal{K}$ are uncovered by the ResDMD algorithm, preserving nonlinearities in the underlying data thanks to using a nonlinear dictionary and providing residuals for associated modes. For this study, an initial value of $N = 2000$ basis functions was used for each pressure gradient case from $M_1 = 2000$ snapshots of the first experiment. Then having built up these basis functions ('dictionary' for the dataset) using kernelized DMD, the algorithm is applied to $M_2 = 24000$ snapshots from the second experiment. Figure 24 shows the eigenvalues for each case against a the unit circle.

The vertical axis in Figure 24 represents the real component of the eigenvalues, while the vertical axis represent their imaginary counterparts. Each eigenvalue is shaded with a different color based on their associated residuals. The eigenvalues represent the growth or decay of each mode. A mode far from the unit circle usually represents transient behavior. Conversely, modes near the edge of the unit circle reflect the system's long-lasting behavior. With the decomposition performed and a preliminary analysis of the eigenvalues and residues for each case's modes, a criteria for observing coherent structures in specific modes can be specified. To do so, one must take into account several properties that a mode may have:

- Reliable modes with small residual, i.e., modes with residuals smaller than 0.2. Picking modes with small residuals, as opposed to picking high energy modes, can lead to much more efficient and accurate representations of the system (see Section 8 of [25]).
- Significant proportions of the modal energy of the remaining modes. This modal energy is taken as the square of the normalized projection of the Koopman matrix onto the observable.
- Significant relative energy of an individual mode. This is defined as the percentage of the total modal energy carried amongst the 200 modes with the smallest residual.

To find such modes, a scatter diagram is shown for each case that compares the residuals and relative energies of the remaining modes after filtering.

In Figure 25 we uncover our first use of ResDMD to investigate the effects of the different pressure gradients. As the pressure gradient increases, the high energy modes shift towards the left region of low residuals. The modes carrying more energy tend to have structures that move faster than the mean velocity. Furthermore, modes with lower residuals tend to have more coherent structures since they are responsible for long-lasting behavior. This suggests that the larger structures in the adverse pressure gradient case may travel in a relatively more unpredictable manner. A more uniform energy distribution across modes with an even larger residual range in the favorable pressure gradient case. A deeper analysis of the key modes, selected based on their modal energy, demonstrates that these modes move comparatively faster relative to their respective mean velocities, when compared with the other modes. When compared to Figures 20 and 22, a much higher magnitude is observed for the favorable pressure gradient than the adverse pressure gradient.

The mode with the highest energy percentage from each case in Figure 25 is chosen and interesting features are observed. These modes are plotted in Figure 26. The superstructures are observed in each figure, all moving faster

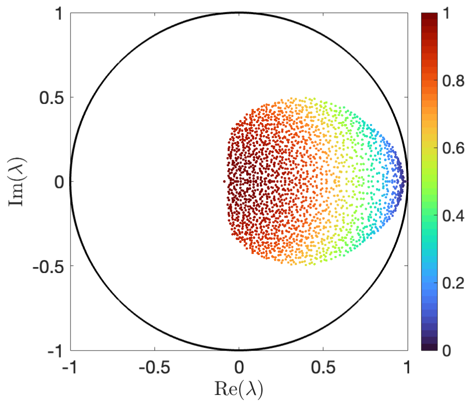

(a) Eigenvalues and associated residuals for the FPG case.

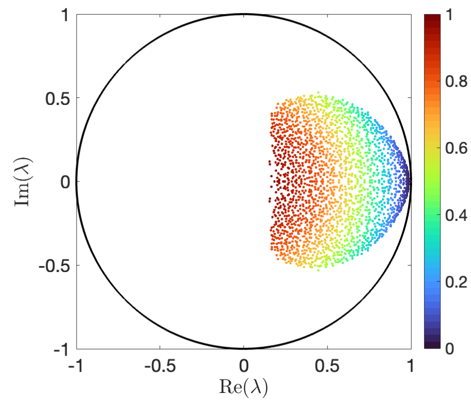

(b) Eigenvalues and associated residuals for the SPG case.

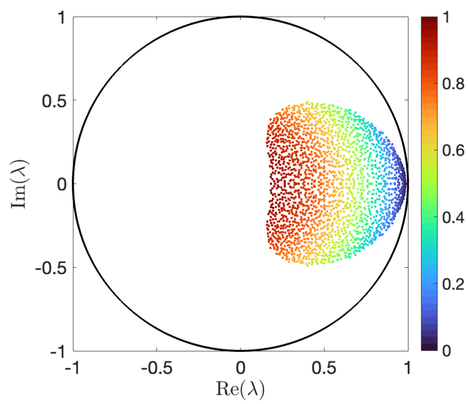

(c) Eigenvalues and associated residuals for the APG case.

Fig. 24 Modal eigenvalues and associated residuals against the unit circle.

relative to the mean velocity. In each case, we see that the eigenvalues are reasonably close to the unit circle, representing long-lasting events in our flow. With more refinement of the methods used to pick modes, we may be able to highlight even more important features of the underlying temporal dynamics observed in each case, so that we may compare and contrast them.

Having demonstrated the unique capability of ResDMD to pick out the desired features of the flow field, a further validation of the algorithm is presented by comparing the spectral measure (see section 4 of [25]) calculated by the algorithm, to the power-spectrum of the streamwise velocity i.e., $S_{uu}(\omega)$. The power spectrum has been normalized with the edge velocity and the boundary layer thickness for a direct comparison. The spectral measure $\nu_{g,N_{ac}}$ from equation (4.13) of [25] can be thought of as a discretized approximation of the power spectrum S_{uu} that reduces the issue of broadening. Figure 27 shows agreement of the two quantities in the moderate frequency range, capturing the $-5/3$ decay for all pressure gradient cases. However, at the lower-frequencies, clear broadening effects are visible for the spectra calculated using the velocity measurements, as they get suppressed in this region, whereas this is not observed for the spectra calculated using the ResDMD analysis. A discussion on the reduced broadening effects of such results has previously been covered in [25].

In the future, a minimal data approach is planned to replicate other important statistical quantities, such as the wavenumber-frequency spectrum of the velocity and pressure fluctuations [32], while further investigating the importance of the transient high-energy modes. This may help to further our understanding of the fast-moving superstructures and the underlying physics, and aid in creating prediction models for their variation with varying pressure gradients. However, the results presented here validate the algorithm and show promise for future applications of this novel modal decomposition technique.

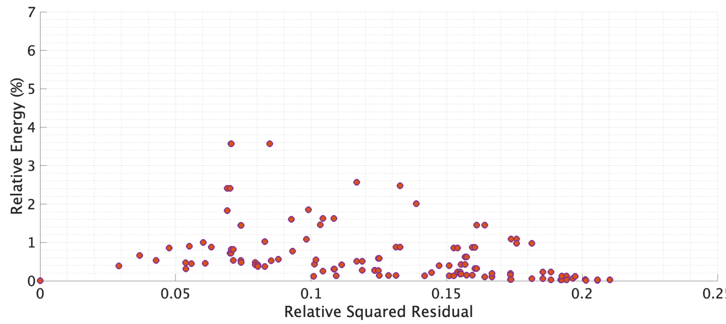

(a) Relative Squared Residual vs Relative Energy for the FPG case.

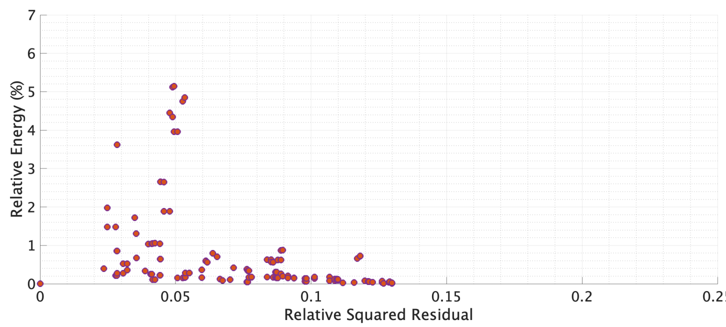

(b) Relative Squared Residual vs Relative Energy for the SPG case.

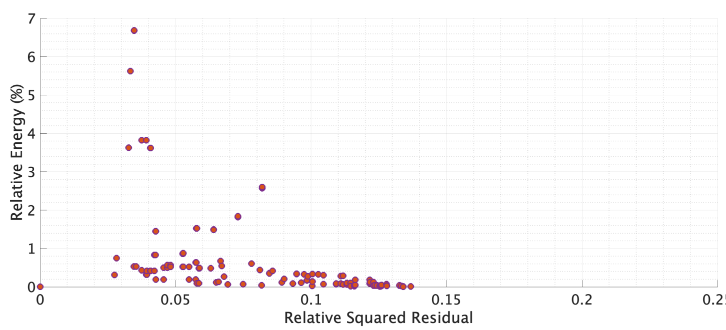

(c) Relative Squared Residual vs Relative Energy for the APG case.

Fig. 25 Scatter plots for each case of the 100 modes with the lowest residuals against their modal energy as a percentage of the total energy held by all these modes.

V. Conclusion

The near-wall large-scale coherent structures were targeted for this study to unveil the sources of low-wavenumber surface pressure fluctuations over a smooth wall. Wall-parallel planar (2D2C) time-resolved PIV measurements were taken at a plane that grazed the smooth wall at $Re_\tau \approx 3500$. Three different mean-pressure gradient cases were compared and studied at the same freestream Reynolds number, providing varying boundary layer characteristics and streamwise and spanwise Reynolds stresses. The streamwise Reynolds stresses were found to be slightly lower than predicted by the wall-normal PIV data acquired in the same flow conditions earlier. This could be attributed to the wall-grazing height of the measurement plane and the averaging nature within the thickness of the laser sheet. The spanwise Reynolds stresses showed the effects of significant filtering in the spanwise direction, causing it to attenuate to only about a third of the streamwise Reynolds stresses.

Results showed the presence of very large streamwise-oriented coherent structures that were on the order of 1-20δ. Large-scale high-speed structures were separated by even larger slow-moving structures in the streamwise direction as

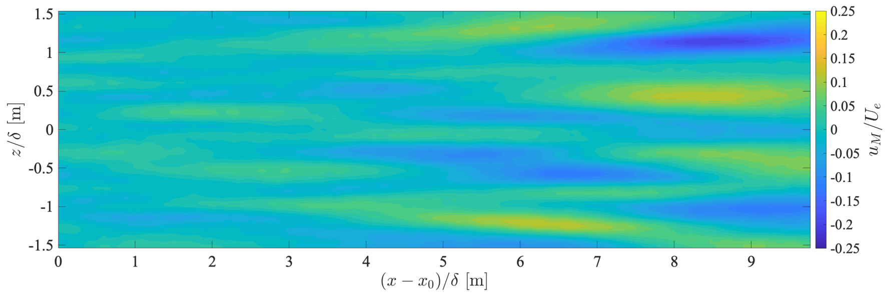

(a) Streamwise modal velocity contours for the FPG case. Specific mode contains 3.57% of the total filtered modal energy, has eigenvalue $\lambda = 0.9571 - 0.0669i$ and residual $\tau_N(\lambda) = 0.0796$.

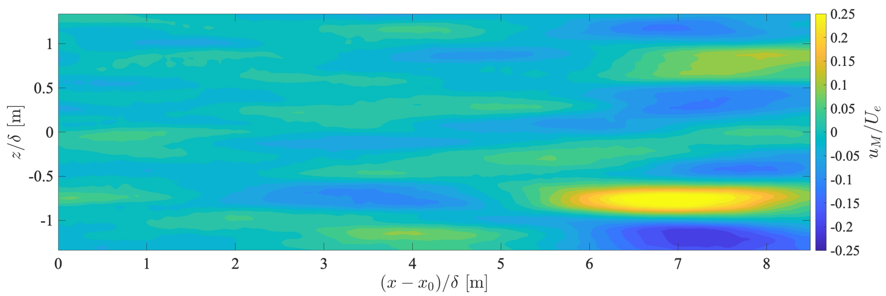

(b) Streamwise velocity contours for the SPG case. Specific mode contains 5.14% of the total filtered modal energy, has eigenvalue $\lambda = 0.9714 + 0.00534i$ and residual $\tau_N(\lambda) = 0.0607$.

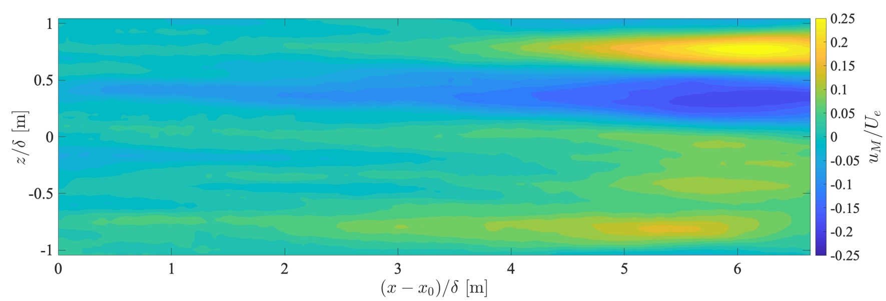

(c) Streamwise velocity contours for the APG case. Specific mode contains 6.69% of the total filtered modal energy, has eigenvalue $\lambda = 0.9785 + 0.0096i$ and residual $\tau_N(\lambda) = 0.024$.

Fig. 26 Modal Mean-subtracted streamwise velocity normalized with the edge velocity for each pressure gradient case (chosen based on energy content and residuals).

they meander downstream with different bulk velocities. The physical characteristics of these structures, such as their streamwise length scales, time scales, separation widths, were found to be pressure-gradient dependent. For instance, the anchored spatial correlations showed an increase in the overall extent of the spatial correlation coefficient as the pressure gradient varied from favorable to adverse. Specifically, when β increased from -0.292 to +0.409, the extent of the correlated region ($\rho_{uu} = 0.1$) increased by 25.9% in the streamwise and 61.9% in the spanwise direction. Similarly, the spanwise separation of the negatively correlated bands increased by 57% for the same variation in the pressure gradient. However, upon normalizing these characteristics using the boundary layer's outer parameters (U_e, δ, δ^*), a neat collapse

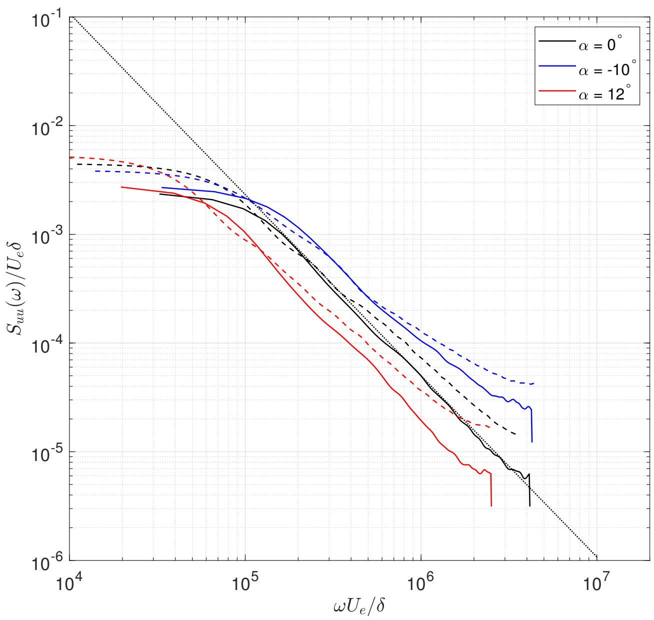

Fig. 27 Comparisons of $S_{uu}(\omega)$ for experimental data (solid lines) and ResDMD approximations (dashed lines) for every pressure gradient case.

was exhibited. This suggested the dependence of these spatial statistics on the outer boundary layer parameters. The comparison of the length scales in the streamwise and the spanwise direction also confirmed the strong anisotropy of the flow, biased towards the streamwise direction. The streamwise integral length-scales of the streamwise velocity were found to be about 65-85% of the boundary layer's thickness, whereas the spanwise length-scales were about 6-8%.

The wavenumber-frequency spectra between the wall-pressure and velocity fluctuations for the three pressure-gradient cases were also compared. The asymmetrical distribution of spectral level about the convective ridge was observed to be biased towards the subconvective region. The subconvective region was significantly dominant for the FPG case compared to the other cases. These elevated levels suggested the importance and dominant contributions of the low-wavenumber turbulence. The corresponding pressure spectra indicated similar behavior as the velocity spectra, hinting towards a stronger connection between the large-scale coherence within turbulent boundary layers and low-wavenumber wall-pressure fluctuations.

Residual Dynamic Mode Decomposition (ResDMD) was utilized to compare and contrast the three pressure gradient cases. First, energy distribution was investigated and residuals were assigned to the corresponding modes within the flow. ResDMD identified a key trend regarding the distribution of energy across the key modes (filtered for low residuals and hence high reliability). It was identified that more energetic modes are present within the lowest residual modes for the APG case, suggesting more long-lasting modes contain structures moving with a higher velocity than the mean. At the same time, the converse is true for the FPG case. The ability of the ResDMD algorithm to pick out the flow structures based on their length and time-scales was demonstrated. This was done for the three pressure gradients under consideration. Evidence of increased spanwise meandering for the APG case, as compared to the FPG case was provided and discussed. It was also shown that by selecting the appropriate ResDMD modes, the fast moving (relative to mean) superstructures could be identified, which can be critical to develop further understanding of the subconvective region.

In summary, results were presented to quantify the turbulence characteristics of the large-scale coherence in turbulent boundary layers with the motivation to isolate the low-wavenumber sources of the wall-pressure fluctuations. Although a strong correlation is presented by comparing the pressure spectra with the velocity spectra in the subconvective domain, identifying the exact turbulent events still remains a challenge. It is important to remember that correlation does not necessarily suggest causation and the data must be interpreted carefully. In order to have the liberty of directly relating the turbulent events in a boundary layer, such as the convection of a large-scale coherent structure, the velocity measurements must be taken synchronously with the pressure measurements. While these results warrant further investigation, they still confirm several essential features of near-wall turbulent boundary layers, which can provide a basis for the studies to follow.

Acknowledgments

The authors would like to thank the Office of Naval Research (ONR), Dr. Ki Han Kim and Dr. Julie Young for their continued support under the grant N00014-20-2821 and N00014-22-1-2729. The authors are also thankful to the Virginia Tech Stability Wind Tunnel support, including Dr. Aurelien Borgoltz and Mr. Bill Oetjens. Special Thanks to Vidya Vishwanathan for her continued support in various aspects of the experiment. M.J.C. would like to thank the LMS for a Cecil King Travel Scholarship that funded a visit to Virginia Tech. Lastly, the team is grateful for the efforts put in by the machine shop at the Aerospace and Ocean Engineering Department at Virginia Tech, led by Mr. James Lambert and Mr. Cameron Hollandsworth.

References

[1] Glegg, S., and Devenport, W., *Aeroacoustics of low Mach number flows: fundamentals, analysis, and measurement*, Academic Press, 2017.

[2] Willmarth, W. W., "Wall pressure fluctuations in a turbulent boundary layer," *The Journal of the Acoustical Society of America*, Vol. 28, No. 6, 1956, pp. 1048–1053.

[3] Kraichnan, R. H., "Pressure fluctuations in turbulent flow over a flat plate," *The Journal of the Acoustical Society of America*, Vol. 28, No. 3, 1956, pp. 378–390.

[4] Corcos, G. M., "The structure of the turbulent pressure field in boundary-layer flows," *Journal of Fluid Mechanics*, Vol. 18, No. 3, 1964, pp. 353–378. https://doi.org/10.1017/S002211206400026X.

[5] Chase, D. M., "Modeling the wavevector-frequency spectrum of turbulent boundary layer wall pressure," *Journal of Sound and Vibration*, Vol. 70, No. 1, 1980, pp. 29–67. https://doi.org/doi.org/10.1016/0022-460X(80)90553-2.

[6] Chase, D. M., "The character of the turbulent wall pressure spectrum at subconvective wavenumbers and a suggested comprehensive model," *Journal of Sound and Vibration*, Vol. 112, No. 1, 1987, pp. 125–147. https://doi.org/doi.org/10.1016/S0022-460X(87)80098-6.

[7] Graham, W. R., "A comparison of models for the wavenumber-frequency spectrum of turbulent boundary layer pressures," *Shock and Vibration Digest*, Vol. 30, No. 2, 1998.

[8] Blake, W. K., *Mechanics of flow-induced sound and vibration, Volume 2: Complex flow-structure interactions*, Academic press, 2017.

[9] Damani, S., Butt, H., Banks, J. T., Srivastava, S., Balantrapu, N. A., Lowe, T., and Devenport, W. J., *Low-Wavenumber Wall Pressure Measurements in Zero-Pressure Gradient Boundary Layer Flow*, 2022. https://doi.org/10.2514/6.2022-1795.

[10] Butt, H., Damani, S., Srivastava, S., Banks, J. T., Vishwanathan, V., Devenport, W. J., Lowe, T., and Glegg, S. A., *Pressure Gradient Effects on Low-Wavenumber Wall-Pressure Fluctuations in Turbulent Boundary Layer Flows*, ???? https://doi.org/10.2514/6.2022-2803.

[11] Grant, H. L., "The large eddies of turbulent motion," *Journal of Fluid Mechanics*, Vol. 4, No. 2, 1958, pp. 149–190. https://doi.org/10.1017/S0022112058000379.

[12] Blake, W. K., "Turbulent boundary-layer wall-pressure fluctuations on smooth and rough walls," *Journal of Fluid Mechanics*, Vol. 44, No. 4, 1970, pp. 637–660. https://doi.org/10.1017/S0022112070002069.

[13] Kovasznay, L. S. G., "The Turbulent Boundary Layer," *Annual Review of Fluid Mechanics*, Vol. 2, No. 1, 1970, pp. 95–112. https://doi.org/10.1146/annurev.fl.02.010170.000523.

[14] Townsend, A., *The structure of turbulent shear flow*, Cambridge university press, 1980.

[15] Zhou, J., Adrian, R. J., and Balachandar, S., "Autogeneration of near-wall vortical structures in channel flow," *Physics of Fluids*, Vol. 8, No. 1, 1996, pp. 288–290.

[16] Kim, K. C., and Adrian, R. J., "Very large-scale motion in the outer layer," *Physics of Fluids*, Vol. 11, No. 2, 1999, pp. 417–422. https://doi.org/10.1063/1.869889.

[17] del Alamo, J. C., and Jimenez, J., "Spectra of the very large anisotropic scales in turbulent channels," *Physics of Fluids*, Vol. 15, No. 6, 2003, p. L41. https://doi.org/10.1063/1.1570830.

[18] Ganapathisubramani, B., Longmire, E. K., and Marusic, I., "Characteristics of vortex packets in turbulent boundary layers," *Journal of Fluid Mechanics*, Vol. 478, 2003, pp. 35–46. https://doi.org/10.1017/S0022112002003270.

[19] Ganapathisubramani, B., Hutchins, N., Hambleton, W. T., Longmire, E. K., and Marusic, I., "Investigation of large-scale coherence in a turbulent boundary layer using two-point correlations," *Journal of Fluid Mechanics*, Vol. 524, 2005, pp. 57–80. https://doi.org/10.1017/S0022112004002277.

[20] Hutchins, N., and Marusic, I., "Large-scale influences in near-wall turbulence," *Philosophical Transactions of the Royal Society A: Mathematical, Physical and Engineering Sciences*, Vol. 365, No. 1852, 2007, pp. 647–664. https://doi.org/doi:10.1098/rsta.2006.1942.

[21] Hutchins, N., and Marusic, I., "Evidence of very long meandering features in the logarithmic region of turbulent boundary layers," *Journal of Fluid Mechanics*, Vol. 579, 2007, pp. 1–28. https://doi.org/10.1017/S0022112006003946.

[22] Kevin, K., Monty, J., and Hutchins, N., "The meandering behaviour of large-scale structures in turbulent boundary layers," *Journal of Fluid Mechanics*, Vol. 865, 2019, p. R1. https://doi.org/10.1017/jfm.2019.131, URL https://www.cambridge.org/core/article/meandering-behaviour-of-largescale-structures-in-turbulent-boundary-layers/C10AABB5652C1D0061711204727F922D.

[23] Colbrook, M., "The foundations of infinite-dimensional spectral computations," Ph.D. thesis, University of Cambridge, 2020.

[24] Colbrook, M. J., and Townsend, A., "Rigorous data-driven computation of spectral properties of Koopman operators for dynamical systems," *arXiv preprint arXiv:2111.14889*, 2021.

[25] Colbrook, M. J., Ayton, L. J., and Szőke, M., "Residual dynamic mode decomposition: robust and verified Koopmanism," *Journal of Fluid Mechanics*, Vol. 955, 2023, p. A21.

[26] Devenport, W. J., and Lowe, K. T., "Equilibrium and non-equilibrium turbulent boundary layers," *Progress in Aerospace Sciences*, Vol. 131, 2022, p. 100807.

[27] Schetz, J. A., and Bowersox, R. D., *Boundary layer analysis*, American Institute of Aeronautics and Astronautics, 2011.

[28] Hutchins, N., Nickels, T. B., Marusic, I., and Chong, M., "Hot-wire spatial resolution issues in wall-bounded turbulence," *Journal of Fluid Mechanics*, Vol. 635, 2009, pp. 103–136.

[29] Gatti, D., Stroh, A., Frohnapfel, B., and Örlü, R., "Spatial resolution issues in rough wall turbulence," *Experiments in Fluids*, Vol. 63, No. 3, 2022, p. 63. https://doi.org/10.1007/s00348-022-03412-x, URL https://doi.org/10.1007/s00348-022-03412-x.

[30] Vishwanathan, V., Fritsch, D., Lowe, T. K., and Devenport, W. J., "Analysis of coherent structures over a smooth wall turbulent boundary layer in pressure gradient using spectral proper orthogonal decomposition," *AIAA Aviation 2021 Forum*, 2021, p. 2893.

[31] Brunton, S. L., Budišić, M., Kaiser, E., and Kutz, J. N., "Modern Koopman Theory for Dynamical Systems," *SIAM Review*, Vol. 64, No. 2, 2022, pp. 229–340.

[32] Colbrook, M. J., "The mpEDMD algorithm for data-driven computations of measure-preserving dynamical systems," *SIAM Journal on Numerical Analysis*, to appear.